Virus-induced cell gigantism and asymmetric cell division in archaea

Junfeng Liu, Virginija Cvirkaite-Krupovic, Diana P. Baquero, Yunfeng Yang, Qi Zhang, Yulong Shen, Mart Krupovic

BIOLOGICAL SCIENCES: Microbiology

Virus-induced cell gigantism and asymmetric cell division in Archaea

Short title: Cell cycle manipulation by an archaeal virus

Junfeng Liu[a,b], Virginija Cvirkaite-Krupovic[a], Diana P. Baquero[a], Yunfeng Yang[b], Qi Zhang[c], Yulong Shen[b]*, Mart Krupovic[a]*

[a] Archaeal Virology Unit, Institut Pasteur, 75015 Paris, France
[b] CRISPR and Archaea Biology Research Center, State Key Laboratory of Microbial Technology, Microbial Technology Institute, Shandong University, 266237 Qingdao, China
[c] Faculty of Life Science and Technology, Kunming University of Science and Technology, 650500 Kunming, China

* – Correspondence to:
Mart Krupovic
Archaeal Virology Unit,
Department of Microbiology, Institut Pasteur,
75015 Paris, France
E-mail: mart.krupovic@pasteur.fr

Yulong Shen
CRISPR and Archaea Biology Research Center,
State Key Laboratory of Microbial Technology,
Microbial Technology Institute,
Shandong University,
266237 Qingdao, China
E-mail: yulgshen@sdu.edu.cn

Keywords: Archaea, archaeal viruses, asymmetric cell division, budding, ESCRT system, *Bicaudaviridae*, Sulfolobus tengchongensis spindle-shaped virus 2, *Saccharolobus*

ABSTRACT

Archaeal viruses represent one of the most mysterious parts of the global virosphere, with many virus groups sharing no evolutionary relationship to viruses of bacteria or eukaryotes. How these viruses interact with their hosts remains largely unexplored. Here we show that nonlytic lemon-shaped virus STSV2 interferes with the cell cycle control of its host, hyperthermophilic and acidophilic archaeon *Sulfolobus islandicus*, arresting the cell cycle in the S phase. STSV2 infection leads to transcriptional repression of the cell division machinery, which is homologous to the eukaryotic endosomal sorting complexes required for transport (ESCRT) system. The infected cells grow up to 20-fold larger in size, have 8,000-fold larger volume compared to noninfected cells, and accumulate massive amounts of viral and cellular DNA. Whereas noninfected *Sulfolobus* cells divide symmetrically by binary fission, the STSV2-infected cells undergo asymmetric division, whereby giant cells release normal-sized cells by budding, resembling the division of budding yeast. Reinfection of the normal-sized cells produces a new generation of giant cells. If the CRISPR-Cas system is present, the giant cells acquire virus-derived spacers and terminate the virus spread, whereas in its absence, the cycle continues, suggesting that CRISPR-Cas is the primary defense system in *Sulfolobus* against STSV2. Collectively, our results show how an archaeal virus manipulates the cell cycle, transforming the cell into a giant virion-producing factory.

SIGNIFICANCE STATEMENT

Studies on bacterial and eukaryotic viruses have revealed a range of strategies used by viruses to subdue host cells for efficient virus replication. How archaeal viruses interact with their hosts remains largely unknown. We characterize a new strategy employed by a nonlytic archaeal virus STSV2 to transform its host into a giant virion-producing factory, whereby the virus infection blocks normal cell division by binary fission, leading to gradual cell growth to unprecedented sizes. The giant infected cells divide asymmetrically by budding, replenishing the pool of susceptible hosts. Thus, although tinkering with the cell cycle is a common practice among evolutionarily unrelated viruses from different domains of life, the mechanisms and manifestation of these actions can be highly diverse and unexpected.

INTRODUCTON

Viruses and cells have likely coexisted since the emergence of the first living organisms (1). In this context, viruses have evolved a spectrum of infection strategies, with some eliciting almost no detectable impact on the physiology of the cell and others extensively reprogramming the host metabolism for maximal progeny production (2-4). Many eukaryotic viruses have been shown to be master manipulators of cell cycle, subverting it to their advantage by tinkering with specific steps of the cycle (5, 6). For instance, some viruses induce a G1-to-S phase transition in order to replicate their genomes concomitantly with the synthesis of cellular chromosomes, whereas others arrest the progression from the G2 phase, a period of rapid cell growth and protein synthesis, to the M phase during which cells divide (5). Occasionally, virus-mediated deregulation of the cell cycle has dramatic consequences, including development of certain types of cancer (7). Whether viruses of prokaryotes, bacteria and archaea, which represent the dominant part of the global virosphere (8-11), also actively manipulate the cell cycle of their hosts remains largely unknown. Although some bacteriophages have been shown to block cell division (12-14), the reproductive benefits of this action are not always apparent.

In archaea, the cell cycle has been most extensively investigated in hyperthermophiles of the genus *Sulfolobus* (phylum Crenarchaeota), which grow optimally at ~80°C and pH 3. Similar to eukaryotes, an exponentially growing *Sulfolobus* cell goes through (i) a pre-replicative growth period called the G1 phase, (ii) the chromosome replication stage – the S phase, (iii) a second period of cellular growth, G2 phase, and (iv) rapid genome segregation and cell division periods, known as the M and D phases, respectively (15). Cell division in *Sulfolobus* is mediated by the eukaryotic-like ESCRT (endosomal sorting complexes required for transport) machinery, which consists of protein CdvA, four ESCRT-III proteins – ESCRT-III (CdvB), ESCRT-III-1 (CdvB1), ESCRT-III-2 (CdvB2) and ESCRT-III-3 (CdvB3) – and the AAA+ ATPase Vps4 (16-19). The ESCRT-III proteins and Vps4 are homologous to the eukaryotic counterparts, whereas CdvA is specific to archaea.

One of the remarkable features of hyperthermophilic archaea is the diversity of their viruses, most of which do not show structural or genomic relatedness to viruses of bacteria or eukaryotes (20-22). Most of the genes in these virus genomes encode unique proteins of unknown function (23). However, recent studies have uncovered that some of these genes encode diverse anti-CRISPR proteins (24, 25), which allow viruses to subvert the CRISPR-Cas systems, the primary antiviral defense mechanism in archaea (26, 27). Unlike most bacteriophages but similar to viruses of eukaryotes, many archaeal viruses are non-lytic and can be continuously released from the infected cells (21). However, how such viruses transform their hosts into virion-producing factories – sometimes referred to as the virocells (3) – and how virus replication is coordinated with the cell cycle and anti-viral defense mechanisms remains largely unknown. Notably, transcriptomic studies have shown that upon infection with certain archaeal viruses, genes encoding ESCRT proteins can be either upregulated or downregulated (28, 29), suggesting the existence of an interplay between virus infection and cell cycle in archaea. In the case of lytic Sulfolobus turreted icosahedral virus, overexpression of *escrt* genes was linked to virion assembly (30), whereas downregulation of the *escrt* genes during non-lytic Sulfolobus tengchongensis spindle-shaped virus 2 (STSV2) remained unexplained (28, 31).

Here we show that upon STSV2 infection, expression of all ESCRT machinery components is repressed but the growth of the infected cells continues, yielding cells with up to ~20× larger diameters and ~8000× larger volumes compared to non-infected cells. The giant cells serve as virion factories producing infectious viral particles in the course of days, until eventual collapse. Remarkably, the gigantic infected cells underwent asymmetric cell division in an ESCRT-dependent manner, spawning normal-sized cells, which upon reinfection produced a new generation of giant cells, locking the system in a cyclic process. However, in the presence of an active CRISPR-Cas system, new spacers targeting the virus were acquired within the giant cells and the released normal-sized cells were immune to virus infection, and eventually took over the population. Collectively, our results show that an archaeal virus tinkers with the cell cycle, inducing cell

gigantism and asymmetric cell division reminiscent of that occurring in budding yeast. Furthermore, we provide evidence that CRISPR adaptation takes place in productively infected cells, providing new insights into CRISPR-Cas response in archaea.

RESULTS

STSV2 infection induces cell gigantism

To study virus-host interactions in archaea and to investigate the potential link between cell cycle and virus infection, we focused on the non-lytic virus STSV2 (31) and its host, *S. islandicus* REY15A (32). The cells were infected using a multiplicity of infection (MOI) of 10 and the growth dynamics of infected and non-infected cells was followed for up to 10 days by measuring the optical density (OD_{600}) of the corresponding cultures. Virus infection resulted in substantial growth retardation (Figure S1A), which was accompanied with continuous increase in the virus titer until 7 days post infection (dpi; Figure S1B). Although no cell lysis was observed, we could establish a plaque test for STSV2 (Figure S1C), which was used for virus enumeration in subsequent infection experiments. Notably, 7 dpi, there was a steep increase in the optical density of the infected culture, suggesting the emergence of a population of cells resistant to STSV2 infection (see below). Consistently, the titer of the virus in the culture started to decrease. The non-infected cell culture reached the maximal density after 3 days of incubation and entered into the death phase, characterized by gradual lysis (Figure S1A), likely due to consumption of all available nutrients.

To gain further understanding on the progression of the infection, aliquots collected at different time points post-infection were observed using bright-field microscopy. Unexpectedly, we found that STSV2 infection resulted in dramatic increase in the host cell size (Figure 1A). After 1 dpi, the infected cells became more than twice bigger in diameter compared to the non-infected control and progressively enlarged up to 20 μm in diameter (Figure 1A, Figure S1D). By contrast, the average diameter (1.2 ± 0.3 μm) of non-infected cells remained constant (Figure S1E). The integrity of the giant cells was further validated by scanning electron microscopy, which revealed the presence of numerous STSV2 virions on the cell surface (Figure 1B).

To quantify the changes in the infected population, we estimated the fractions of cells with different diameters at different time points post infection. For convenience, we refer to all cells with a diameter of more than 2 μm ($d > 2$ μm) as 'big' cells and those with a diameter of no more than 2 μm ($d \leq 2$μm) as 'normal' cells. As shown in Figure 1C, after 1 dpi, only ~16% of cells were of normal size ($d \leq 2$μm), whereas ~80% of the cells had a diameter ranging from 2 to 4 μm, and about 4% had a diameter between 4 and 8 μm. The overall ratio of normal and big cells was highly reproducible and remained stable (around 20% and 80%, respectively) from 1 to 6 dpi, although the number of cells with larger diameters increased in a time-dependent manner. The fraction of cells with diameters greater than 12 μm reached maximum (~5% of all cells) at 6 dpi (Figure 1C). However, starting with 7 dpi, the overall ratio began to change. Namely, the number of normal ($d \leq 2$μm) and big ($d > 2$μm) cells became roughly equal after 7 dpi and after 8 dpi, the cell culture was dominated by normal-sized cells (96%) (Figure 1C).

To investigate whether the ability to induce cell gigantism is unique to STSV2, we infected REY15A cells with two other non-lytic viruses, Sulfolobus spindle-shaped virus 2 (SSV2; Figure S2A) (33) and Sulfolobus monocaudavirus 1 (SMV1; Figure S2B) (34), both of which can efficiently replicate in REY15A cells. SMV1 is only distantly related to STSV2, although both viruses are tentative members of the family *Bicaudaviridae*, whereas SSV2 belongs to an unrelated virus family, the *Fuselloviridae* (23). SSV2 infection did not induce any changes in cell dimensions discernable by bright-field microscopy (Figure S2C). By contrast, infection with SMV1 led to increase in cell size, similar to that described above for STSV2, albeit SMV1-infected cells did not grow as large as those infected with STSV2 (Figure S2D & 2E). Collectively, these results indicate that bicaudaviruses have a dramatic effect on the biology of their host, leading to an unprecedented increase in cell size. The fact that this phenomenon is not induced by

SSV2 suggests that the process is virus-specific and does not represent a general cell response to virus infection.

STSV2-infected giant cells contain increased DNA content

In asynchronous *Sulfolobus* population, most cells are in G2 phase (>50% of the cell cycle) and contain two copies (2C) of the chromosome, whereas in G1 phase, which is considerably shorter (<5% of the cell cycle), cells contain only one copy (1C) of the chromosome (35). The DNA content in the population can be readily assessed by flow cytometry, which produces characteristic profiles (15, 18). Thus, to characterize the infected population and to investigate what happens with the cellular DNA content during STSV2 infection, we performed flow cytometry analysis. As expected, during the first two days of active growth, the majority of non-infected cells contained two chromosomes (Days 1-2; Figure 2A). However, during the stationary growth stage (Figure S1A), the population became dominated by cells with 1C DNA content (Day 3; Figure 2A), signifying the arrest in G1 phase, potentially due to nutrient limitation. Finally, when the population progressed into the death phase (Days 4-8, Figure S1A), the DNA was gradually degraded, with the peaks of the DNA content shifting from right to the left (Figure 2A).

The profiles of DNA content in STSV2-infected cultures were radically different. After 1 dpi, around 80% of the infected cells contained more than 4C equivalents of DNA, and about 10% of the cells showed the DNA content of less than 1C. As the infection progressed, there appeared cells containing even larger number of DNA copy equivalents (Figure 2A), with some of the giant cells harboring the DNA content corresponding to more than 300 copies (Figure 2B). Over time, the population appeared as a continuum of cells with highly variable DNA contents. Indeed, sorting of individual cells labeled with fluorescent DNA-binding dye (propidium iodide) allowed us to visualize this continuum (Figure 2B). Notably, starting with 2 dpi, we observed appearance of cells with DNA content lower than one chromosome copy, which could correspond to either partially degraded cellular DNA, viral DNA or both. Starting with 6 dpi, two peaks corresponding to 1C and 2C DNA content, characteristic of non-infected cells, started to reappear in infected cells, and became dominant at 8 dpi (Figure 2A). This result is consistent with the observation that 8 dpi the population became dominated by normal-sized cells (Figure 1A, 1C, S1A).

To get further information on the viral and cellular DNA content during the infection, we collected the infected cells at different time points (1-9 dpi), extracted the total (viral+cellular) DNA and performed qPCR with chromosome- and virus-specific primers. The ratio between the viral and cellular genome copy numbers increased gradually, peaking at 6 dpi with ~800 viral genome copies to 1 cellular chromosome copy (Fig. S3A). Following the emergence of resistant cells, the viral-to-host genome ratio decreased sharply. To estimate whether both the viral and cellular genomes were replicated in the big cells, we sorted the infected cells by flow cytometry and collected those with diameters larger than 5 μm (from ~6 to ~16 μm, median diameter 9.45 μm) for qPCR analysis. Knowing the exact cell number, we determined average numbers of viral and cellular genome copy numbers per cell. The big cells, on average, harbored 111 ± 62 copies of the cellular chromosome and 2426 ± 261 copies of the viral genome per cell (Fig. S3B). These results clearly show that both the viral and cellular genomes are replicated during the infection.

To gain insights into the intracellular organization of the DNA, the non-infected and STSV2-infected cells were stained with DAPI and analyzed by confocal microscopy. Regardless of the cell diameter (1-10 μm), the DNA was evenly distributed in the cytoplasm, with no obvious condensation foci (Figure 2C). The 3D reconstruction of the infected cells also confirmed the integrity and spherical morphology of the big cells.

Expression of cell division genes is severely downregulated upon STSV2 infection

The microscopy and flow cytometry data suggest that in STSV2-infected cells, synthesis of the components of cell envelope and DNA replication continue, but the cell division is blocked. Thus, to analyze the expression of the genes involved in cell division throughout the infection, we performed quantitative reverse-transcription PCR (qRT-PCR) with primers specific to all six components of the *Sulfolobus* ESCRT

machinery. A housekeeping gene encoding the TATA-binding protein (TBP) was used as a control. The expression level in the T0 culture (Day 0) was considered as unity and expression levels at other time points were plotted relative to this level. In non-infected cells, the transcription levels of the ESCRT genes were relatively stable, and fluctuated around 1 during exponential and stationary growth stages (Days 1-4; Figure 3A). However, starting with Day 5, the total RNA in the non-infected cells started to be degraded (Figure S4A), consistent with cell lysis and DNA degradation (Figure 2A, S1A). By contrast, in STSV2-infected cells, the RNA remained stable throughout the experiment (Figure S4B). qRT-PCR analysis showed that the transcription levels of all ESCRT machinery components in the infected cells were down-regulated, reaching the lowest levels at 2 dpi (Figure 3B). Expression of the gene encoding ESCRT-III-2 was most severely affected, with 57-fold decrease after 1 dpi, and 1000-fold decrease after 2 dpi (Figure 3B). Notably, expression level of TBP remained stable throughout the experiment, except for the temporary increase at 1 dpi. Importantly, the transcription level of all ESCRT components was stable during days 3-6 dpi, whereas after 7-8 dpi, when the culture became dominated by normal-sized cells, the expression level of the cell division genes reached the level of non-infected control cells (Figure 3B). Consistent with the derepression of the transcription of the ESCRT machinery components, there was a rapid increase in cell division, as can be judged from the increase in optical density (Figure S1A).

To further confirm the link between the cell division genes and cell diameter, we expressed in REY15A cells the C-terminally truncated ESCRT-III and CdvA proteins (ESCRT-IIIΔC and CdvAΔC, respectively), both of which have a negative effect on cell division (17, 36), and observed the cell morphology using bright-field microscopy. In both cases, the cell diameter increased from 1.2 ± 0.3 μm to 4-5 μm (Figure S5A). To more directly mimic the downregulation of the expression of the cell division genes, we depleted the ESCRT-III and CdvA transcripts by 30% and 70%, respectively, using the CRISPR-based knockdown system (37). Cells with up to 4 μm in diameter were observed (Figure S5B). Notably, however, neither approach yielded cells as big as those infected with STSV2, possibly due to additive effect of simultaneous repression of all cell division genes in the case of virus infection. These results further support the link between the repression of the cell division genes and remarkable increase in the dimensions of STSV2-infected cells.

Giant cells release normal-sized cells through asymmetric cell division

As mentioned above, the fraction of normal-sized cells remained around 20% throughout several days of the experiment (Figure 1C), suggesting dynamic renewal of the normal-sized cells. To gain insights into this process, we analyzed the population by bright-field microscopy and observed that some of the infected 'big' cells displayed surface bulges (Figure S6A). Cell sorting by flow cytometry followed by fluorescence microscopy (Figure S6B) as well as confocal microscopy and 3D reconstruction (Supplementary video 1) further suggested that the bulges are an integral part of the big cells, rather than normal-sized cells co-localizing with the big cells. Finally, the continuity between the big cells and the bulges was confirmed by electron microscopy (Figure S6C). In terms of dimensions (~1-1.5 μm) and shape, these bulges resembled the normal-sized cells present in the population. Thus, we hypothesized that the bulges represent budding of normal-sized cells from the big cells, a phenomenon superficially resembling the asymmetric cell division of budding yeast (Figure S6D).

Cell division in *Sulfolobus* occurs by binary fission and depends on the archaeal ESCRT machinery (15, 17, 38-43). To analyze if *Sulfolobus* ESCRT system participates in the formation of budding-like structures in STSV2-infected cells, we performed fluorescence microscopy with antibodies against ESCRT-III-1, one of the three *Sulfolobus* ESCRT-III homologs previously shown to participate in *S. islandicus* REY15A cell division (17). In non-infected cells, ESCRT-III-1 formed ring-like structures in the mid-cell at different stages of cell division, including cytokinesis whereby the membrane is constricted between the two daughter cells (Figure 4A). No such mid-cell ring-like structures could be detected in the STSV2-infected big cells, in which ESCRT-III-1 formed only small dot-like foci (Figure S7). However, when the STSV2-infected cells contained the 'buds', ESCRT-III-1 became organized into ring- or spiral-like structures,

which localize at the budding sites (Figure 4B). These results strongly suggest that the normal-sized cells are produced by the 'big' cells through a budding or asymmetric cell division mechanism, thereby replenishing the subpopulation of normal-sized cells, and that ESCRT machinery participates in this process.

STSV2-infected cells develop CRISPR-based resistance

As mentioned above, after 8 dpi, the normal-sized cells outnumbered the big cells (Figure 1), which coincided with the derepression of the cell division genes (Figure 3) and sharp increase in the optical density of the culture (Figure S1A). We hypothesized that the observed changes in the infected population resulted from emergence of cells resistant to the STSV2 infection. CRISPR-Cas system is the most extensively studied antiviral mechanism of *Sulfolobus* and has been shown to be effective against different viruses and plasmids (24, 34, 44-47). *S. islandicus* REY15A carries two CRISPR loci, three distinct CRISPR interference modules (one type IA and two type IIIB systems) and a single adaptation module, which integrates virus-derived spacers into both CRISPR loci (32, 45) (Figure S8A). Notably, a previous study has failed to detect spacer acquisition from STSV2, unless the cells were co-infected with SMV1 (44).

To analyze if de novo CRISPR adaptation occurred in the course of STSV2 infection, we amplified the leader-proximal regions of both CRISPR loci at different time points post infection. PCR products corresponding to newly acquired spacers were observed in both CRISPR loci starting with 7 dpi (Figure S9A). Notably, the bands corresponding to the ancestral CRISPR loci were also visible, albeit much fainter, suggesting that at all times the population was a mixture of cells with and without spacers against STSV2. To verify that the new spacers were indeed acquired from STSV2, the infected culture after 10 dpi was plated on solid medium and three colonies of cells with a variable number of spacers (S1-S3) in both CRISPR loci (Figure S9B) were selected for isolation. Sequencing of the leader-proximal regions of CRISPR1 and CRISPR2 loci of S1-S3 has confirmed that the newly acquired spacers are derived from STSV2 (Figure S8B). Spot assay has shown that all three strains are resistant to STSV2 (Figure S8C). To further confirm this result, S2 strain was infected with STSV2 in liquid culture and observed by bright-field microscopy; no appreciable changes in cell morphology or size were detected (Figure S9D), consistent with the resistance to STSV2 infection. Collectively, these results demonstrate that STSV2 infection is countered by the CRISPR-Cas system and leads to de novo acquisition of multiple new spacers targeting STSV2. To study what happens with the viral genome in STSV2 spacer-containing cells, we infected spacer-lacking (REY15A) and spacer-containing (S2) strains and tracked the presence of the STSV2 genome by PCR. Whereas STSV2 genome accumulated in the *wt* cells (Figure S9E), it was degraded in the S2 cells (Figure S9F). The STSV2 genome-specific band started to diminish at 10 hours post infection and became barely detectable after 2 dpi. These results strongly suggest that CRISPR targeting leads to degradation of the STSV2 genome.

Given that normal-sized cells are released by budding from the big cells, the STSV2-targeting CRISPR spacers could be acquired either in productively infected big cells or directly in the normal-sized cells potentially upon infection with defective viruses, as has been demonstrated for certain bacteriophages (48). To distinguish between the two possibilities, we sorted the infected cells using flow cytometry into populations of $d \leq 2\mu m$ and $d > 5\mu m$ at different time points post infection, and analyzed the collected populations for the presence of new CRISPR spacers by PCR, as described above. The newly acquired spacers were detected not only in the normal-sized cells (Figure S9G) but also in the big cells (Figure S9H), indicating that CRISPR adaptation could take place in cells successfully infected with STSV2. Consequently, normal-sized cells budding from the big cells carrying spacers against STSV2 would be resistant to virus infection.

CRISPR-Cas system is indispensable for the emergence of resistant population

To test if resistance to STSV2 infection can emerge by a mechanism independent of the CRISPR-Cas system, e.g., mutation of the receptor, we infected with STSV2 a mutant strain of *S. islandicus* REY15A,

ΔC1C2 (hereinafter ΔCRISPR), bearing a large chromosomal deletion encompassing the only adaptation module, type IA interference module and both CRISPR loci (Figure S8A) (49). Infected ΔCRISPR cells increased in size, similar to the wild-type REY15A cells (Figure S10). However, unlike in the wild-type cells, the resistant population did not emerge. Instead, even after 8 dpi, when the wild-type population was dominated by normal-sized cells ($d \leq 2\mu m$), the number of such cells in the ΔCRISPR culture remained stable at around 20% (Figure 5A). Consistently, there was no increase in the optical density of the ΔCRISPR culture (Figure S1A) nor was there a reappearance of the population with 1C-2C chromosomes detectable by flow cytometry (Figure 5B). These results show that even if cells with CRISPR-independent resistance to STSV2 did emerge in the population, they were below the detection limit during our experiment, allowing the population of big cells to be stably renewed and maintained.

DISCUSSION

Viruses are the master manipulators of their hosts at both cellular and population levels (50). Studies on virus-host interactions have greatly contributed to uncovering many fundamental aspects of cell biology, especially in eukaryotes, including mechanisms of membrane fusion, membrane scission by the ESCRT machinery, apoptosis, cytoskeleton remodeling, functioning of plasmodesmata in plants and many more (51-54). How archaeal viruses affect the biology of their hosts remains largely unknown. Here we described a new phenomenon, whereby an archaeal virus interferes with the cell cycle of its host to orchestrate the transformation of the infected cell into a gigantic virion factory. The 20-fold increase in cell diameter compared to the non-infected spherical *Sulfolobus* cell translates to over 8000-fold increase in cell volume, as can be calculated using a simple formula $4/3\pi r^3$, where r is radius. The volume of a 20 μm cell would be 4.2×10^3 fL (or $4.2 \times 10^3\ \mu m^3$), which is three to four orders of magnitude larger than the volume (~0.4–3 μm^3) of typical model bacteria, such as *Bacillus subtilis*, *Staphylococcus aureus*, *Escherichia coli* and *Caulobacter crescentus* (55). Even many unicellular eukaryotes, such as budding yeast and green algae, are considerably smaller, with the diameters of 3–6 μm (Figure S5D) (56, 57). To the best of our knowledge, such virus-induced increase in cell dimension has not been reported for any other virus. We propose a model whereby the archaeal virus STSV2 manipulates the cell cycle of its host causing cell gigantism and asymmetric cell division (Figure 6).

Diffusion is one of the factors believed to restrict the size of most prokaryotes (58). High surface to internal volume ratio of prokaryotic cells ensures efficient diffusion of nutrients, elimination of waste and the timely movement of biomolecules, alleviating the need for dedicated transport systems found in the larger eukaryotic cells. Indeed, compartmentalization, emergence of motor protein-facilitated trafficking over a complex cytoskeletal network and acquisition of energy-generating organelles have all been credited for the advancement of the size and complexity of eukaryotic cells (55, 58). A prevailing hypothesis posits that eukaryotes have evolved from a lineage of archaea (59, 60). However, most extant archaea, and in particular, the postulated archaeal ancestor of eukaryotes (61), have small cell size. Our results suggest that dramatic increase in cell size and volume can be readily achieved through reprogramming of the preexisting cellular machineries. We obtained similar results with two different archaeal viruses, STSV2 and SMV1, indicating that the observed increase in the cell size is not an artifact. Interestingly, it has been reported that hyperthermophilic crenarchaeon *Staphylothermus marinus*, which belongs to the same class (Thermoprotei) as *Sulfolobus*, upon growth in the presence of high concentrations of yeast extract as the sole substrate increased in diameter from the typical 0.5–1 μm up to 15 μm (62). These observations illuminate the plasticity of archaeal cells, possibly enabled by the absence of rigid peptidoglycan layer found in most bacteria.

The size increase of STSV2-infected cells appears to be linked to the repression of the genes encoding ESCRT machinery components. In synchronized non-infected *Sulfolobus* cells, expression of some of the cell division genes is cell cycle-dependent: whereas Vps4 is expressed throughout the cell cycle, ESCRT-III is nearly undetectable during G1 and S (synthesis) phases and is produced only starting with the G2 phase, when DNA replication is complete (18, 37). In STSV2-infected cells, expression of cell division

genes is severely downregulated, whereas genome replication continues to an extravagant extent, with some cells containing over 300 equivalents of chromosome copies. This state resembles arrest of the cell cycle in S phase. Indeed, a number of eukaryotic viruses, such as hepatitis B virus (63), polyomaviruses and papillomaviruses (64), and adenovirus (65), promote the transition and/or arrest of the cell cycle in the S phase. For small eukaryotic DNA viruses, which do not encode a complete DNA replication machinery, entry into S phase ensures access to the host enzymatic activities and cellular DNA precursors for virus DNA replication (6). Notably, like most crenarchaeal viruses, STSV2 does not encode its own DNA polymerase (31) and thus, in all likelihood, relies on the host machinery for genome replication.

Repression of cell division genes in STSV2-infected cells, although severe, is not total or irreversible and after 2 dpi there is a partial release of the repression, which coincides with increase in the fraction of normal-sized cells in the population to ~20%. Remarkably, whereas non-infected *Sulfolobus* cells invariably divide by binary fission (15-17, 39, 40, 42), in the infected population, normal-sized cells are produced by budding from the giant cells. This mode of cell division has never been described for any archaeon, but is highly reminiscent of the asymmetric cell division characteristic of budding yeast, *Saccharomyces cerevisiae* (66), and that observed during self-renewal and differentiation of stem cells (67) as well as during tumorigenesis (68). The major difference between symmetric and asymmetric cell division lies in the selection of the division site, where the cytokinetic furrow including the ESCRT machinery is assembled (66). Interestingly, like in the case of symmetric cell division, the asymmetric division of STSV2-infected cells appears to be dependent on the action of the ESCRT machinery, consistent with the formation of ESCRT-III-1-containing rings and spiral-like structures in the outgoing budding cells. It is remarkable that the budding cells are of normal size, suggesting the existence of a common mechanism determining the size of the daughter cells in both infected and non-infected cells. Further research will be required to determine the full composition of the division apparatus in the infected cells and the mechanism of its asymmetric positioning. Regardless, our current results, in combination with the recent demonstration that ESCRT system is responsible for the budding of extracellular vesicles in *Sulfolobus* (37), implicate the archaeal ESCRT machinery in membrane remodeling processes beyond membrane abscission during normal cell division by binary fission. Whether the involvement of ESCRT system can be extended to the budding of archaeal viruses (69), including STSV2, as has been demonstrated for diverse enveloped viruses of eukaryotes, such as HIV-1 and Ebola virus (52, 70, 71), remains to be investigated. Topologically, however, the budding of cells (as shown in this study), vesicles and viruses are equivalent processes, whereby ESCRT proteins mediate the so-called 'reverse'-topology membrane scission at the narrow membrane necks contiguous with the cytoplasm (52).

The normal-sized cells released by budding replenish the pool of susceptible hosts and can be re-infected with STSV2 produced in the previous rounds of infection or, alternatively, the infection can be propagated to the daughter cell in the form of virus genomes during the budding process (Figure 6). The latter strategy of infection would be particularly efficient, because the virus would not have to face the harsh extracellular environment and loss (or mutation) of the receptor would not block the virus propagation. Regardless of the mechanism, the outcome of the infection is the same – the newly produced cells again increase in size, yielding the next generation of giant cells. This cycle repeats itself, unless virus resistance develops. During the nine days of our experiment, no such resistance has arisen, unless CRISPR-Cas system was functional. Indeed, in the absence of the CRISPR-Cas system, the ratio of giant and normal-sized cells remained stable, with no signs of resistance development. However, when CRISPR-Cas system was operational, resistant cells emerged 7 dpi, carrying variable number of CRISPR spacers in both CRISPR loci, seeding a resistant population which was maintained during subsequent passages of the culture (Figure S8).

The mechanism of spacer acquisition in archaea has been studied in vitro (72-76) and has been documented during infection with different viruses in vivo (34, 44, 77). However, it remained unclear how CRISPR adaptation is coordinated with the virus infection at the cellular level. That is, are spacer acquisition and anti-virus response sufficiently rapid to save a productively infected cell? In bacteria, it has been shown that replication-deficient phages are responsible for the vast majority of the acquisition of CRISPR-

mediated phage immunity (48). By contrast, infection with virulent, replication-competent phages often results in abortive infection and demise of the infected cells, rather than immunity (78, 79). In the case of STSV2 infection, newly acquired spacers were identified in the giant cells, suggesting that adaptation took place in spite of active virus replication. Resistant cells rapidly took over the population, terminating the virus propagation.

To our knowledge, STSV2 and SMV1 are the first archaeal viruses suggested to manipulate the cell cycle of their host. We have shown that STSV2 infection blocks the normal cell division in *Sulfolobus*, which leads to unprecedented cell growth and asymmetric division reminiscent to that operating in budding yeast. In the presence of CRISPR-Cas system, the population can recover and revert to division by binary fission. The plasticity of *Sulfolobus* cells is remarkable and similar properties could have played a key role during eukaryogenesis. The STSV2-*Sulfolobus* system might serve as a powerful model for addressing fundamental unanswered questions of archaeal cell biology, including transition between binary fission and asymmetric cell division, cell cycle control, determination of the optimal size of the daughter cell, de novo CRISPR adaptation in archaea, and more. As a first step in this direction, it will be important to identify the viral factor(s) responsible for repression of the cell division genes. STSV2 and SMV1 encode several putative transcriptional regulators (31, 34) which could be the prime suspects involved in this process.

MATERIALS AND METHODS

Strains and growth conditions

Strains used in this study are listed in Table S1. *Sulfolobus islandicus* REY15A was grown aerobically at 75°C in TSV medium, as described previously (80). TSV medium supplemented with 0.01% (wt/vol) uracil (U), TSVU, was used for culturing of *S. islandicus* CRISPR deletion mutant ΔC1C2 (49). *Saccharomyces cerevisiae* Y2H Gold strain was grown aerobically at 30°C with shaking (180 rpm) in YPD medium containing 1% (wt/vol) Yeast extract, 2% (wt/vol) peptone and 2% (wt/vol) dextrose.

Infection assays

For infection, REY15A and ΔC1C2 cells were collected at mid-logarithmic phase, and mixed with the virus. The multiplicity of infection (MOI) used for infection was 10. The MOI was calculated based on the plaque assays. The infected cultures were incubated at 75°C for 1h without shaking. Following the incubation, the cells were pelleted and washed with 7% sucrose for three times (7000 rpm for 10 min) to remove the unadsorbed virions. Finally, the infected cells were resuspended in the TSVU medium and incubated at 75°C with shaking (140 rpm). Infections with SSV2 and SMV1 were also carried out at an MOI of 10.

Further details on microscopy and flow cytometry techniques used are provided in SI Methods.

References

1. Krupovic M, Dolja VV, & Koonin EV (2019) Origin of viruses: primordial replicators recruiting capsids from hosts. *Nat Rev Microbiol* 17(7):449-458.
2. Howard-Varona C*, et al.* (2020) Phage-specific metabolic reprogramming of virocells. *ISME J*.
3. Forterre P (2013) The virocell concept and environmental microbiology. *ISME J* 7(2):233-236.
4. Moniruzzaman M, Martinez-Gutierrez CA, Weinheimer AR, & Aylward FO (2020) Dynamic genome evolution and complex virocell metabolism of globally-distributed giant viruses. *Nat Commun* 11(1):1710.
5. Fan Y, Sanyal S, & Bruzzone R (2018) Breaking Bad: How Viruses Subvert the Cell Cycle. *Front Cell Infect Microbiol* 8:396.
6. Bagga S & Bouchard MJ (2014) Cell cycle regulation during viral infection. *Methods Mol Biol* 1170:165-227.
7. Mesri EA, Feitelson MA, & Munger K (2014) Human viral oncogenesis: a cancer hallmarks analysis. *Cell Host Microbe* 15(3):266-282.
8. Danovaro R*, et al.* (2016) Virus-mediated archaeal hecatomb in the deep seafloor. *Sci Adv* 2(10):e1600492.
9. Breitbart M, Bonnain C, Malki K, & Sawaya NA (2018) Phage puppet masters of the marine microbial realm. *Nat Microbiol* 3(7):754-766.
10. Dion MB, Oechslin F, & Moineau S (2020) Phage diversity, genomics and phylogeny. *Nat Rev Microbiol* 18(3):125-138.
11. Mushegian AR (2020) Are There 10(31) Virus Particles on Earth, or More, or Fewer? *J Bacteriol* 202(9):e00052-00020.
12. Haeusser DP*, et al.* (2014) The Kil peptide of bacteriophage lambda blocks Escherichia coli cytokinesis via ZipA-dependent inhibition of FtsZ assembly. *PLoS Genet* 10(3):e1004217.
13. Stewart CR, Deery WJ, Egan ES, Myles B, & Petti AA (2013) The product of SPO1 gene 56 inhibits host cell division during infection of Bacillus subtilis by bacteriophage SPO1. *Virology* 447(1-2):249-253.
14. Kiro R*, et al.* (2013) Gene product 0.4 increases bacteriophage T7 competitiveness by inhibiting host cell division. *Proc Natl Acad Sci U S A* 110(48):19549-19554.
15. Lindås AC & Bernander R (2013) The cell cycle of archaea. *Nat Rev Microbiol* 11(9):627-638.
16. Samson RY, Duggin IG, & Bell SD (2019) Analysis of the Archaeal ESCRT Apparatus. *Methods Mol Biol* 1998:1-11.
17. Liu J*, et al.* (2017) Functional assignment of multiple ESCRT-III homologs in cell division and budding in Sulfolobus islandicus. *Mol Microbiol* 105(4):540-553.
18. Samson RY, Obita T, Freund SM, Williams RL, & Bell SD (2008) A role for the ESCRT system in cell division in archaea. *Science* 322(5908):1710-1713.
19. Lindås AC, Karlsson EA, Lindgren MT, Ettema TJ, & Bernander R (2008) A unique cell division machinery in the Archaea. *Proc Natl Acad Sci U S A* 105(48):18942-18946.
20. Munson-McGee JH, Snyder JC, & Young MJ (2018) Archaeal Viruses from High-Temperature Environments. *Genes (Basel)* 9(3):E128.
21. Prangishvili D*, et al.* (2017) The enigmatic archaeal virosphere. *Nat Rev Microbiol* 15(12):724-739.
22. Krupovic M, Cvirkaite-Krupovic V, Iranzo J, Prangishvili D, & Koonin EV (2018) Viruses of archaea: Structural, functional, environmental and evolutionary genomics. *Virus Res* 244:181-193.
23. Iranzo J, Koonin EV, Prangishvili D, & Krupovic M (2016) Bipartite Network Analysis of the Archaeal Virosphere: Evolutionary Connections between Viruses and Capsidless Mobile Elements. *J Virol* 90(24):11043-11055.
24. Athukoralage JS*, et al.* (2020) An anti-CRISPR viral ring nuclease subverts type III CRISPR immunity. *Nature* 577(7791):572-575.

25. He F, *et al.* (2018) Publisher Correction: Anti-CRISPR proteins encoded by archaeal lytic viruses inhibit subtype I-D immunity. *Nat Microbiol* 3(9):1076.
26. Makarova KS, *et al.* (2020) Evolutionary classification of CRISPR-Cas systems: a burst of class 2 and derived variants. *Nat Rev Microbiol* 18(2):67-83.
27. Mohanraju P, *et al.* (2016) Diverse evolutionary roots and mechanistic variations of the CRISPR-Cas systems. *Science* 353(6299):aad5147.
28. León-Sobrino C, Kot WP, & Garrett RA (2016) Transcriptome changes in STSV2-infected Sulfolobus islandicus REY15A undergoing continuous CRISPR spacer acquisition. *Mol Microbiol* 99(4):719-728.
29. Ortmann AC, *et al.* (2008) Transcriptome analysis of infection of the archaeon Sulfolobus solfataricus with Sulfolobus turreted icosahedral virus. *J Virol* 82(10):4874-4883.
30. Snyder JC, Samson RY, Brumfield SK, Bell SD, & Young MJ (2013) Functional interplay between a virus and the ESCRT machinery in archaea. *Proc Natl Acad Sci U S A* 110(26):10783-10787.
31. Erdmann S, *et al.* (2014) A novel single-tailed fusiform Sulfolobus virus STSV2 infecting model Sulfolobus species. *Extremophiles* 18(1):51-60.
32. Guo L, *et al.* (2011) Genome analyses of Icelandic strains of Sulfolobus islandicus, model organisms for genetic and virus-host interaction studies. *J Bacteriol* 193(7):1672-1680.
33. Stedman KM, *et al.* (2003) Relationships between fuselloviruses infecting the extremely thermophilic archaeon Sulfolobus: SSV1 and SSV2. *Res Microbiol* 154(4):295-302.
34. Erdmann S & Garrett RA (2012) Selective and hyperactive uptake of foreign DNA by adaptive immune systems of an archaeon via two distinct mechanisms. *Mol Microbiol* 85(6):1044-1056.
35. Bernander R & Poplawski A (1997) Cell cycle characteristics of thermophilic archaea. *J Bacteriol* 179(16):4963-4969.
36. Samson RY, *et al.* (2011) Molecular and structural basis of ESCRT-III recruitment to membranes during archaeal cell division. *Mol Cell* 41(2):186-196.
37. Liu J, *et al.* (2021) Archaeal extracellular vesicles are produced in an ESCRT-dependent manner and promote gene transfer and nutrient cycling in extreme environments. *bioRxiv* doi: https://doi.org/10.1101/2021.02.09.430445.
38. Samson RY & Bell SD (2009) Ancient ESCRTs and the evolution of binary fission. *Trends Microbiol* 17(11):507-513.
39. Charles-Orszag A, Lord SJ, & Mullins RD (2020) High-temperature live-cell imaging of cytokinesis, cell motility and cell-cell adhesion in the thermoacidophilic crenarchaeon Sulfolobus acidocaldarius. *bioRxiv* doi: https://doi.org/10.1101/2020.02.16.951772.
40. Samson RY & Bell SD (2011) Cell cycles and cell division in the archaea. *Curr Opin Microbiol* 14(3):350-356.
41. Samson RY, Dobro MJ, Jensen GJ, & Bell SD (2017) The Structure, Function and Roles of the Archaeal ESCRT Apparatus. *Subcell Biochem* 84:357-377.
42. Tarrason Risa G, *et al.* (2020) The proteasome controls ESCRT-III-mediated cell division in an archaeon. *Science* 369(6504):eaaz2532.
43. Pulschen AA, *et al.* (2020) Live Imaging of a Hyperthermophilic Archaeon Reveals Distinct Roles for Two ESCRT-III Homologs in Ensuring a Robust and Symmetric Division. *Curr Biol* 30(14):2852-2859 e2854.
44. Erdmann S, Le Moine Bauer S, & Garrett RA (2014) Inter-viral conflicts that exploit host CRISPR immune systems of Sulfolobus. *Mol Microbiol* 91(5):900-917.
45. Deng L, Garrett RA, Shah SA, Peng X, & She Q (2013) A novel interference mechanism by a type IIIB CRISPR-Cmr module in Sulfolobus. *Mol Microbiol* 87(5):1088-1099.
46. He F, Vestergaard G, Peng W, She Q, & Peng X (2017) CRISPR-Cas type I-A Cascade complex couples viral infection surveillance to host transcriptional regulation in the dependence of Csa3b. *Nucleic Acids Res* 45(4):1902-1913.

47. Manica A & Schleper C (2013) CRISPR-mediated defense mechanisms in the hyperthermophilic archaeal genus Sulfolobus. *RNA Biol* 10(5):671-678.
48. Hynes AP, Villion M, & Moineau S (2014) Adaptation in bacterial CRISPR-Cas immunity can be driven by defective phages. *Nat Commun* 5:4399.
49. Gudbergsdottir S*, et al.* (2011) Dynamic properties of the Sulfolobus CRISPR/Cas and CRISPR/Cmr systems when challenged with vector-borne viral and plasmid genes and protospacers. *Mol Microbiol* 79(1):35-49.
50. Roux S & Brum JR (2019) A viral reckoning: viruses emerge as essential manipulators of global ecosystems. *Environ Microbiol Rep* 11(1):3-8.
51. Hay S & Kannourakis G (2002) A time to kill: viral manipulation of the cell death program. *J Gen Virol* 83(Pt 7):1547-1564.
52. Schöneberg J, Lee IH, Iwasa JH, & Hurley JH (2017) Reverse-topology membrane scission by the ESCRT proteins. *Nat Rev Mol Cell Biol* 18(1):5-17.
53. Reagan BC & Burch-Smith TM (2020) Viruses Reveal the Secrets of Plasmodesmal Cell Biology. *Mol Plant Microbe Interact* 33(1):26-39.
54. Walsh D & Naghavi MH (2019) Exploitation of Cytoskeletal Networks during Early Viral Infection. *Trends Microbiol* 27(1):39-50.
55. Levin PA & Angert ER (2015) Small but Mighty: Cell Size and Bacteria. *Cold Spring Harb Perspect Biol* 7(7):a019216.
56. Vander Wiel JB*, et al.* (2017) Characterization of Chlorella vulgaris and Chlorella protothecoides using multi-pixel photon counters in a 3D focusing optofluidic system. *Rsc Adv* 7(8):4402-4408.
57. Ahmad MR, Nakajima M, Kojima S, Homma M, & Fukuda T (2008) The effects of cell sizes, environmental conditions, and growth phases on the strength of individual W303 yeast cells inside ESEM. *IEEE Trans Nanobioscience* 7(3):185-193.
58. Schulz HN & Jorgensen BB (2001) Big bacteria. *Annu Rev Microbiol* 55:105-137.
59. Zaremba-Niedzwiedzka K*, et al.* (2017) Asgard archaea illuminate the origin of eukaryotic cellular complexity. *Nature* 541(7637):353-358.
60. López-García P & Moreira D (2020) The Syntrophy hypothesis for the origin of eukaryotes revisited. *Nat Microbiol* 5(5):655-667.
61. Imachi H*, et al.* (2020) Isolation of an archaeon at the prokaryote-eukaryote interface. *Nature* 577(7791):519-525.
62. Fiala G, Stetter KO, Jannasch HW, Langworthy TA, & Madon J (1986) *Staphylothermus marinus* sp. nov. represents a novel genus of extremely thermophilic submarine heterotrophic archaebacteria growing up to 98 °C. *Syst Appl Microbiol* 8(1-2):106-113.
63. Benn J & Schneider RJ (1995) Hepatitis B virus HBx protein deregulates cell cycle checkpoint controls. *Proc Natl Acad Sci U S A* 92(24):11215-11219.
64. Shadan FF, Cowsert LM, & Villarreal LP (1994) n-Butyrate, a cell cycle blocker, inhibits the replication of polyomaviruses and papillomaviruses but not that of adenoviruses and herpesviruses. *J Virol* 68(8):4785-4796.
65. Bagchi S, Raychaudhuri P, & Nevins JR (1990) Adenovirus E1A proteins can dissociate heteromeric complexes involving the E2F transcription factor: a novel mechanism for E1A trans-activation. *Cell* 62(4):659-669.
66. Bhavsar-Jog YP & Bi E (2017) Mechanics and regulation of cytokinesis in budding yeast. *Semin Cell Dev Biol* 66:107-118.
67. Berika M, Elgayyar ME, & El-Hashash AH (2014) Asymmetric cell division of stem cells in the lung and other systems. *Front Cell Dev Biol* 2:33.
68. Knoblich JA (2010) Asymmetric cell division: recent developments and their implications for tumour biology. *Nat Rev Mol Cell Biol* 11(12):849-860.

69. Quemin ER*, et al.* (2016) Eukaryotic-like virus budding in Archaea. *mBio* 7(5):e01439-01416.
70. Hurley JH & Cada AK (2018) Inside job: how the ESCRTs release HIV-1 from infected cells. *Biochem Soc Trans* 46(5):1029-1036.
71. Vietri M, Radulovic M, & Stenmark H (2020) The many functions of ESCRTs. *Nat Rev Mol Cell Biol* 21(1):25-42.
72. Grainy J, Garrett S, Graveley BR, & M PT (2019) CRISPR repeat sequences and relative spacing specify DNA integration by Pyrococcus furiosus Cas1 and Cas2. *Nucleic Acids Res* 47(14):7518-7531.
73. Shiimori M, Garrett SC, Graveley BR, & Terns MP (2018) Cas4 Nucleases Define the PAM, Length, and Orientation of DNA Fragments Integrated at CRISPR Loci. *Mol Cell* 70(5):814-824 e816.
74. Rollie C, Graham S, Rouillon C, & White MF (2018) Prespacer processing and specific integration in a Type I-A CRISPR system. *Nucleic Acids Res* 46(3):1007-1020.
75. Rollie C, Schneider S, Brinkmann AS, Bolt EL, & White MF (2015) Intrinsic sequence specificity of the Cas1 integrase directs new spacer acquisition. *Elife* 4:e08716.
76. Garrett S*, et al.* (2020) Primed CRISPR DNA uptake in Pyrococcus furiosus. *Nucleic Acids Res* 48(11):6120-6135.
77. Li M, Wang R, Zhao D, & Xiang H (2014) Adaptation of the Haloarcula hispanica CRISPR-Cas system to a purified virus strictly requires a priming process. *Nucleic Acids Res* 42(4):2483-2492.
78. Watson BNJ*, et al.* (2019) Type I-F CRISPR-Cas resistance against virulent phages results in abortive infection and provides population-level immunity. *Nat Commun* 10(1):5526.
79. Strotskaya A*, et al.* (2017) The action of Escherichia coli CRISPR-Cas system on lytic bacteriophages with different lifestyles and development strategies. *Nucleic Acids Res* 45(4):1946-1957.
80. Deng L, Zhu H, Chen Z, Liang YX, & She Q (2009) Unmarked gene deletion and host-vector system for the hyperthermophilic crenarchaeon Sulfolobus islandicus. *Extremophiles* 13(4):735-746.

Acknowledgements

This work was supported by National Key R&D Program of China [2020YFA0906800] and National Natural Science Foundation of China [31970546, 31670061] to Y.S.; l'Agence Nationale de la Recherche (grant ENVIRA, #ANR-17-CE15-0005-01) and Emergence(s) project MEMREMA from Ville de Paris to M.K.; PRESTIGE post-doctoral program from European Union's Seventh Framework Programme and the National Key Research and Development Program of China (No. 2020YFA0906800) to J.L. The authors would like to thank Pierre-Henri Commere from Flow Cytometry Platform of Institut Pasteur for the help with cell sorting as well as Christine Schmitt and Olivier Gorgette from UTechS UBI of Institut Pasteur for their help with scanning electron microscopy. We are also grateful to the Ultrastructural BioImaging (UTechS UBI) unit of Institut Pasteur for access to electron microscopes. We gratefully acknowledge the UtechS Photonic BioImaging (Imagopole), C2RT, Institut Pasteur, supported by the French National Research Agency (France BioImaging; ANR-10-INSB-04; Investments for the Future), for access to confocal microscope.

Competing interests

The authors declare no competing interests.

Figures and legends

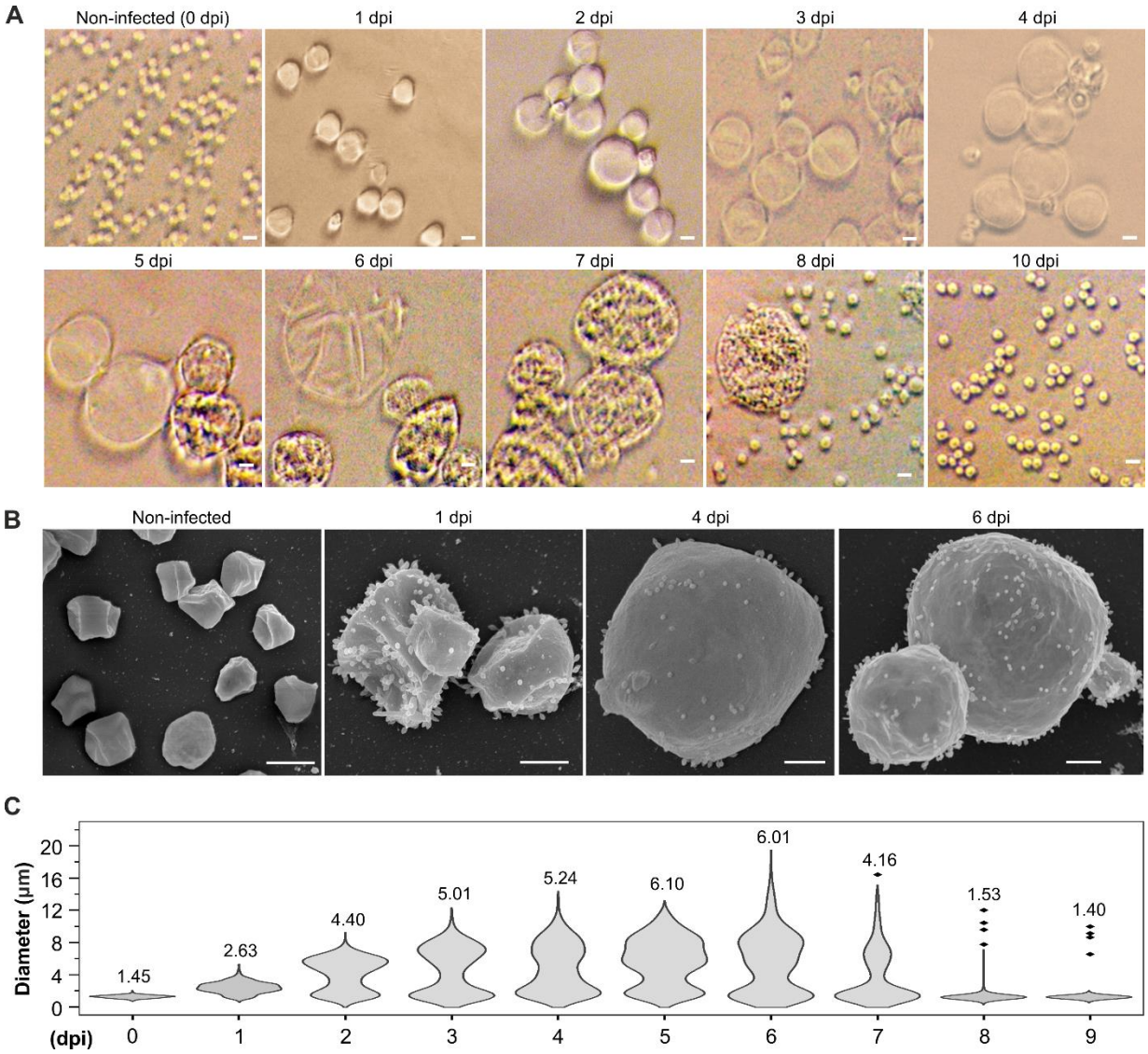

Figure 1. STSV2 infection induces cell gigantism. Differential interference contrast (A) and scanning electron microscopy analysis (B) of noninfected and STSV2-infected REY15A cells. (Scale bars, 2 μm in A and 1 μm in B.) (C) Size distribution of the STSV2-infected REY15A cells during different time points after infection. The numbers above the plots represent median diameters of cells for each time point. Cell cultures were sampled at the indicated time points and the diameters of 600 cells from two independent experiments were measured for each time point using ImageJ (NIH).

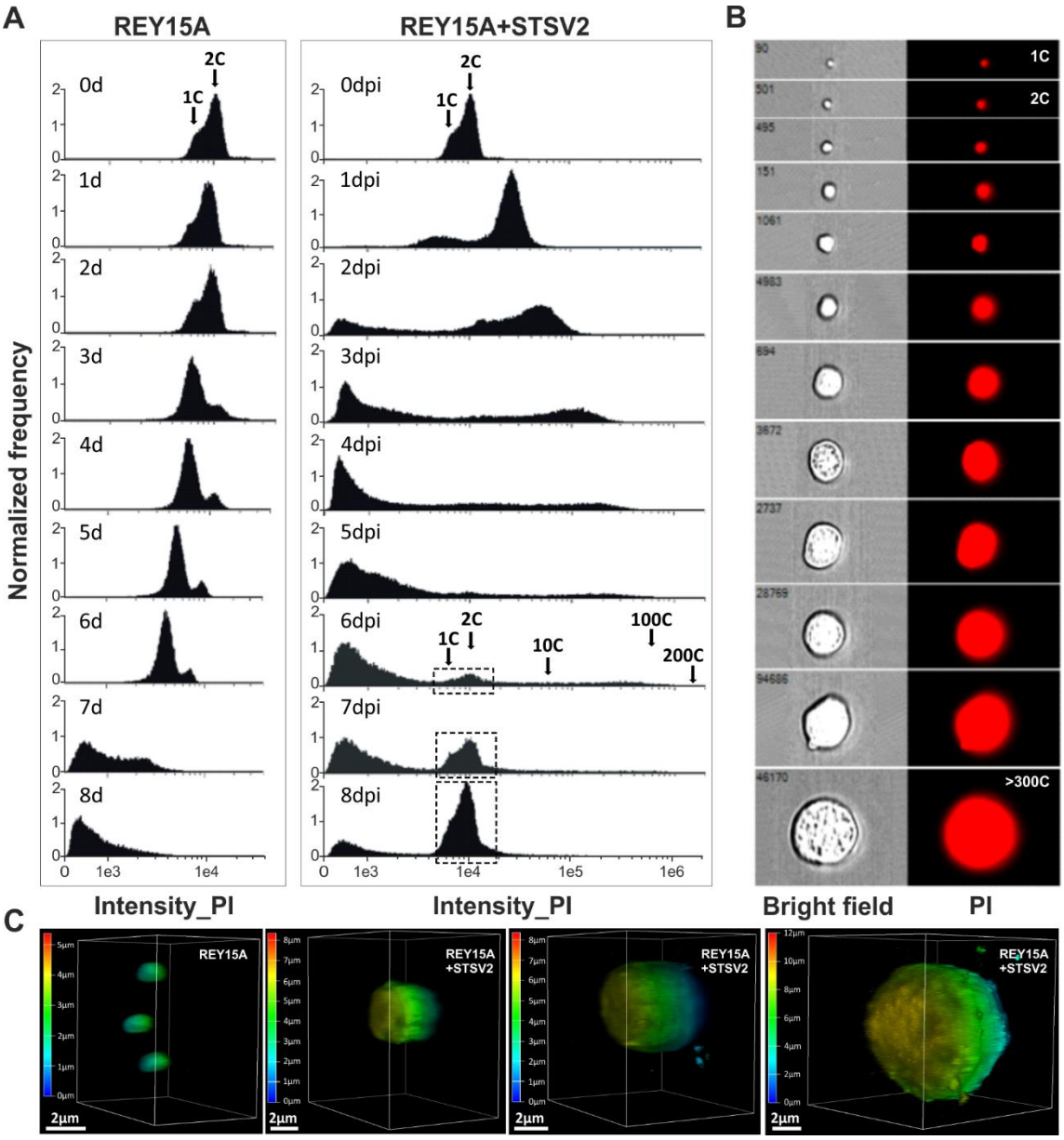

Figure 2. STSV2-infected giant cells contain increased DNA content. (A) Flow cytometry analysis of noninfected (Left) and STSV2-infected (Right) REY15A cells. Cell cultures were sampled and analyzed at the indicated time points. Arrows indicate cells with the DNA content corresponding to the equivalents of 1 copy (1C), 2C, 10C, 100C, and 200C of genomic DNA. The dotted boxes indicate the region of cells containing the DNA content corresponding to 1 and 2 copies, which reappeared in the infected cells at 6 dpi. (B) Representative images showing single cells sorted by flow cytometry with different diameters and DNA content equivalents ranging from 1 copy to more than 300 copies. PI, propidium iodide. (C) Three-dimensional reconstruction images of noninfected and STSV2-infected REY15A cells with different diameters. The cells were stained with DAPI and observed using a Leica SP8 confocal microscope. The images were analyzed by the Leica Application Suite X (LAS X) software and displayed in the volume mode. The color scale indicates the Z-depth. (Scale bars, 2 μm.)

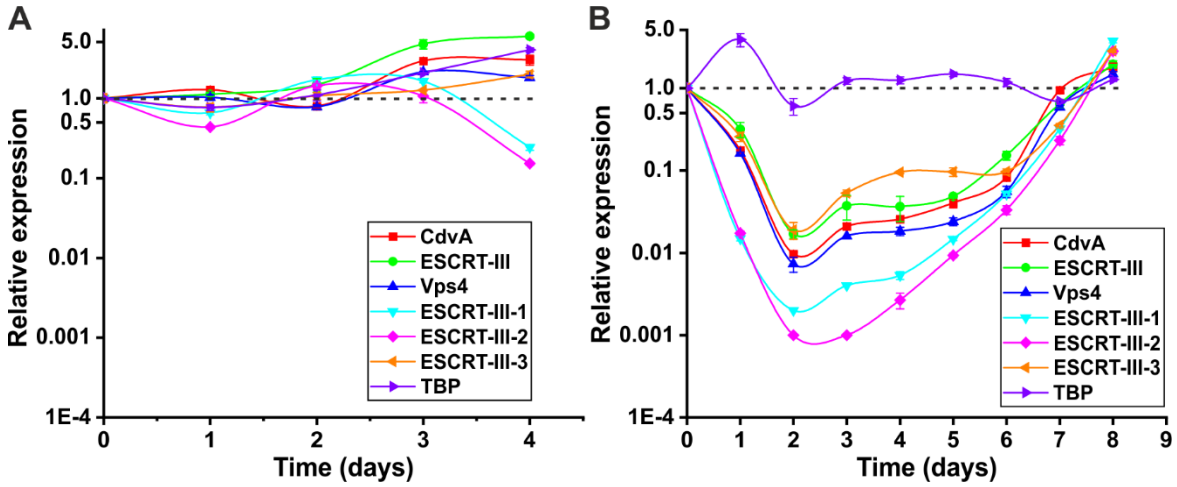

Figure 3. Expression of cell division genes is down-regulated upon STSV2 infection. Transcriptional analysis of noninfected (A) and STSV2-infected (B) REY15A cells. Cell cultures were sampled and analyzed at the indicated time points. 16S rRNA was used as the reference and tbp, a housekeeping gene encoding TATA-binding proteins, was used as the control. The transcription levels of the target genes in the cell cultures at 0 dpi (i.e., noninfected cells prior to infection) were defined as 1 (indicated by the dashed lines). Three biological replicates were analyzed for each time point. Error bars represent SD from three independent experiments.

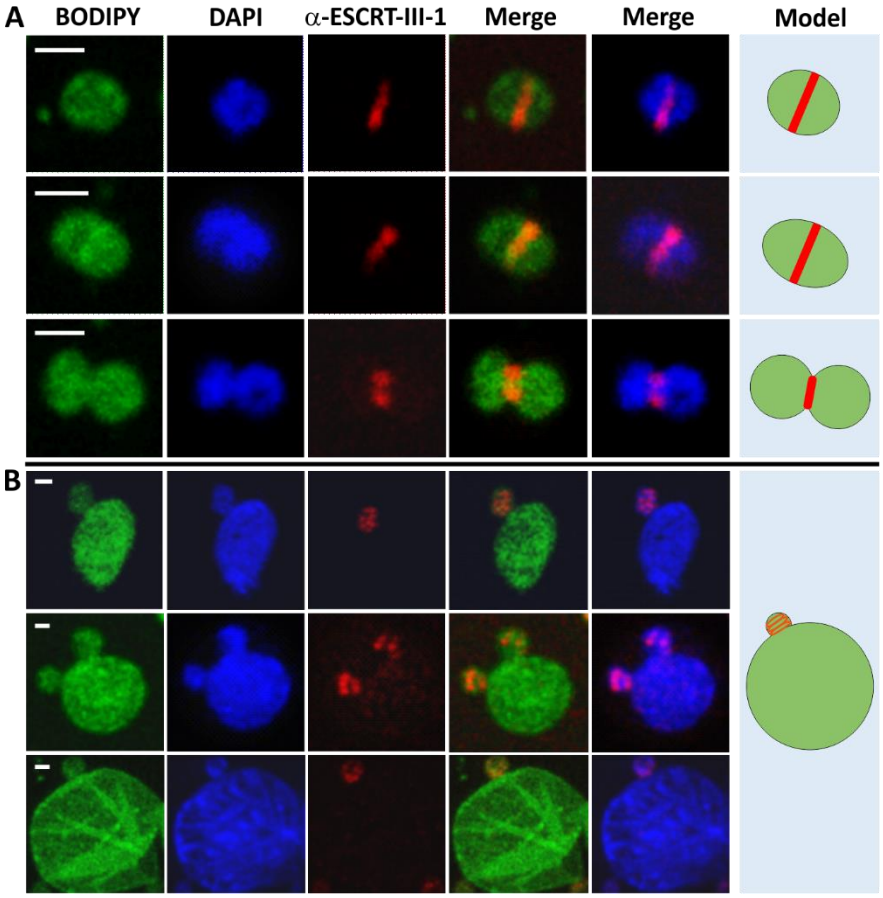

Figure 4. Immunofluorescence microscopy analysis of noninfected and STSV2-infected REY15A cells. (A) Noninfected REY15A cells at different stages of cell division. ESCRT-III-1 localizes at the midcell forming a band-like structure, which constricts with the progression of the cell division process. (B) STSV2-infected cells undergo asymmetric cell division or budding with ESCRT-III-1 localizing at the budding site forming a ring or spiral-like structures. Fixed cells were stained with BODIPY (green) to visualize the membrane, DAPI (blue) to visualize DNA, and fluorescently labeled anti-ESCRT-III-1 antibody (red) to visualize ESCRT-III-1. Hypothetical models are shown on the Right. (Scale bars, 1 μm.)

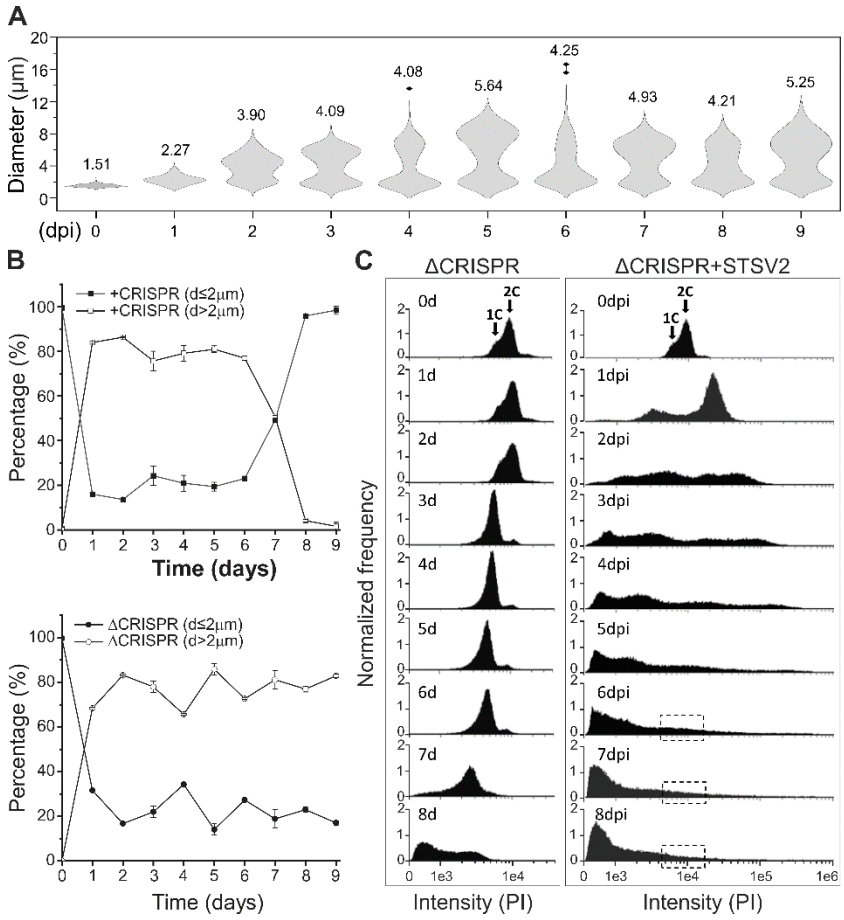

Figure 5. CRISPR-Cas system is indispensable for the emergence of a resistant population. (A) Size distribution of the STSV2-infected CRISPR-deficient ΔC1C2 cells during different time points after infection. The width of the distribution corresponds to the frequency of occurrence. The numbers above the plots represent median diameters of cells during each time point. Cell culture was sampled at the indicated time points and the diameters of 600 cells from two independent experiments were measured at each time point. (B) Changes in the diameter of cells with (Top) and without (Bottom) the CRISPR immune system during STSV2 infection. For convenience of presentation, cells were grouped into two categories—those with d ⩽ 2 μm and those with d > 2 μm. (C) Flow cytometry analysis of the DNA content in the ΔCRISPR mutant during the infection with STSV2. Cell cultures were sampled and analyzed at the indicated time points. Arrows indicate cells with the DNA content corresponding to the equivalents of one and two copies (1C and 2C, respectively) of genomic DNA. The dotted boxes indicate the region corresponding to the DNA content of one and two copies, which reappeared in the CRISPR-containing cell culture (Fig. 2A).

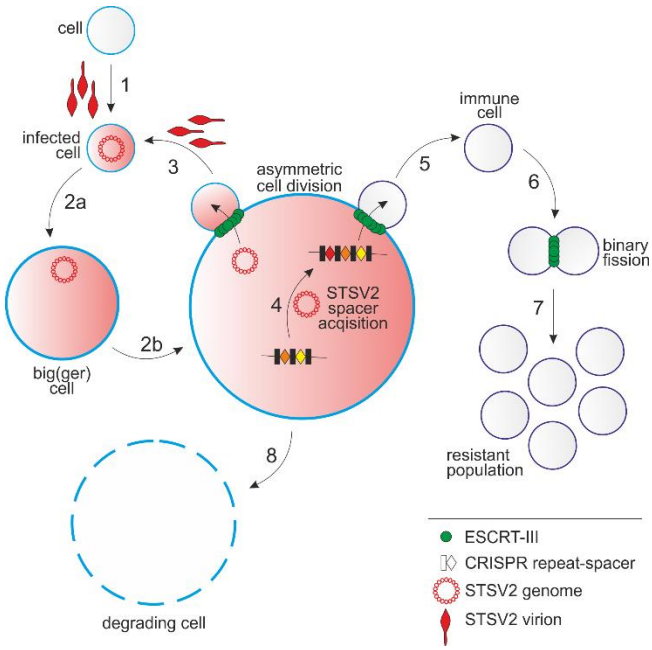

Figure 6. A schematic representation of the STSV2-*Sulfolobus* interactions. 1: infection of a normal-sized cell; 2a and 2b: gradual increase in the diameter of STSV2-infected cells; 3: asymmetric division of a STSV2-infected giant cell leading to the budding of a normal-sized cell, which can be reinfected (by exogenous virus or by virus genome vertically transmitted from the giant cell) to restart the cycle; 4: acquisition of CRISPR spacers against STSV2; 5: asymmetric division of a STSV2-infected giant cell leading to the budding of a normal-sized cell resistant to STSV2 infection due to the presence of CRISPR spacers against STSV2; 6: division of the STSV2-resistant cells by binary fission; 7: proliferation of the resistant population; and 8: gradual decay of the giant cell.

SUPPLEMENTARY INFORMATION

Virus-induced cell gigantism and asymmetric cell division in Archaea

Short title: Cell cycle manipulation by an archaeal virus

Junfeng Liu[a,b], Virginija Cvirkaite-Krupovic[a], Diana P. Baquero[a], Yunfeng Yang[b], Qi Zhang[c], Yulong Shen[b]*, Mart Krupovic[a]*

[a] Archaeal Virology Unit, Institut Pasteur, 75015 Paris, France
[b] CRISPR and Archaea Biology Research Center, State Key Laboratory of Microbial Technology, Microbial Technology Institute, Shandong University, 266237 Qingdao, China
[c] Faculty of Life Science and Technology, Kunming University of Science and Technology, 650500 Kunming, China

* – Correspondence to:
Mart Krupovic
Archaeal Virology Unit,
Department of Microbiology, Institut Pasteur,
75015 Paris, France
E-mail: mart.krupovic@pasteur.fr

Yulong Shen
CRISPR and Archaea Biology Research Center,
State Key Laboratory of Microbial Technology,
Microbial Technology Institute,
Shandong University,
266237 Qingdao, China
E-mail: yulgshen@sdu.edu.cn

This PDF contains
Supplementary Methods
Supplementary Figures S1-S9
Legend for Supplementary video S1
Supplementary Table S1
Supplementary references

SI Methods

Propagation and purification of virus particles

STSV2 was propagated in *S. islandicus* REY15A. A stock of STSV2-infected REY15A cells was inoculated into TSV medium and incubated at 75°C with shaking. When the OD_{600} reached 0.6-0.8, the cell culture was transferred to 4 × 1L TSV medium containing mineral salt solution, 0.2% (wt/vol) tryptone (T), 0.2% (wt/vol) sucrose (S) and a mix of vitamins (V); the pH of medium was adjusted to 3.5 with sulfuric acid. When the OD_{600} reached ~0.8, the cells were removed by centrifugation at 7,000 rpm for 20 min. The supernatant containing STSV2 was first filtered with 0.45 μm filter to remove the remaining cells and cell debris, and then concentrated by the Vivaflow 200 Crossflow cassette (Sartorius Stedim Lab Ltd, Stonehouse, GL10 3UT, UK). STSV2 was further concentrated by ultracentrifugation at 35,000 rpm (Type 50.2 Ti rotor) for 2 h and then resuspended in mineral salt medium. The virus was further purified by sucrose gradient and CsCl gradient ultracentrifugation, and stocked at 4°C until used. Sulfolobus monocaudavirus 1 (SMV1) and Sulfolobus spindle-shaped virus 2 (SSV2) were propagated in the highly susceptible strain, *S. islandicus* CRISPR deletion mutant ΔC1C2 as described previously (1, 2). SMV1 and SSV2 were purified in a similar way as STSV2.

Plaque and spot assays

TS medium supplemented with 0.1% (wt/vol) yeast extract and 0.3% (wt/vol) phytagel was used for plaque assays. The titer of STSV2 was determined by plaque assays. Serial dilutions of the viral preparations (100 μL) were mixed with *S. islandicus* REY15A cells. Then 10 mL pre-heated TSY medium containing 0.3% phytagel was added to the mixture, vortexed and immediately poured into the empty Petri dishes. The plates were incubated at 75°C. After about 1.5 days, visible STSV2 plaques appeared as small clear halos.

For the spot assay, wild type REY15A cells and REY15A cells with different numbers of CRISPR spacers (S1, S2 and S3) were collected at mid-logarithmic phase and mixed with 10 ml of pre-heated TYS medium containing 0.3% (wt/vol) phytagel, vortexed and immediately poured into the empty Petri dishes. After the plates solidified, 5μl of the serially diluted STSV2 preparation were applied on the plates and incubated at 75 °C for 1.5 days.

Bright-field microscopy

5 μl of non-infected and infected cell cultures at indicated time points were examined under an inverted fluorescence microscope (Carl Zeiss, Germany) in differential interference contrast (DIC) mode.

Fluorescence microscopy

Fluorescence microscopy analysis was performed as previously described (3). Briefly, non-infected and STSV2-infected REY15A cells were collected and pelleted down at 6,000 rpm for 5 min, and resuspended in 300 μl PBS buffer (137 mM NaCl, 2.7 mM KCl, 10 mM $Na_2HPO_4 \times 12H_2O$, 2 mM KH_2PO_4). The cells were fixed by adding 700 μl of cold absolute ethanol at 4°C for 2 h. Then the cells were pelleted down and washed with PBST buffer (PBS plus 0.05% Tween-20) for 3 times at 6,000 rpm for 5 min. The primary antibody against ESCRT-III-1 (HuaAn Biotechnology Co., Hangzhou, Zhejiang, China) was added (dilution of 1:1000 in PBST buffer) and incubated at 4°C overnight. The cells were then pelleted down and washed with PBST buffer for 3 times at 6,000 rpm for 5 min. Goat anti-rabbit IGG Alexa Fluor® 568, Invitrogen™ (Thermo Fisher Scientific, USA) was added (dilution of 1:1000 in PBST) and incubated at room temperature for 2 h. Then the cells were pelleted down and washed with PBST buffer for 3 times at 6,000 rpm for 5 min. The cells were finally resuspended in PBS buffer containing BODIPY (Thermo Fisher Scientific, USA) and DAPI (4', 6-diamidino-2-phenylindole) to stain the membrane and DNA, respectively. After 30 min of staining, the samples were observed under a Leica TCS SP8 confocal microscope (Leica, Germany).

For 3D confocal imaging, the live cells from non-infected and STSV2-infected REY15A cultures were collected and pelleted down at 6,000 rpm for 5 min and then resuspended in PBS buffer containing DAPI.

After 30 min of staining, the samples were observed under a Leica TCS SP8 confocal microscope (Leica, Germany) with a z-step of about 0.35-0.45 μm. The 3D confocal series were reconstructed by Leica Application Suite X (LAS X) software (Leica). The 3D volume visualization was shown together with the depth coding to display the depth information. The 3D video was obtained by rotation around Y-axis and then the X-axis with 1.5 times enlargement.

Transmission electron microscopy

For negative-staining TEM analysis, 10 μl of virus preparations or virus-infected cells were adsorbed onto glow-discharged copper grids with carbon-coated Formvar film and negatively stained with 2.0% (w/v) uranyl acetate. The samples were then observed under FEI Tecnai BioTwin 120 microscope (FEI, Einthoven, The Netherlands) operated at 120 kV.

Scanning electron microscopy

Non-infected and STSV2-infected cell cultures were collected at the indicated times and the samples were prepared as described previously (4). The samples were then loaded onto SEM specimen stubs with double adhesive tape and sputter coated with gold. Microscopy analysis was performed under high vacuum mode with 5.0 Kv electron beam using the AURIGA Compact Focused Ion Beam Scanning Electron Microscope (Carl ZEISS, Germany).

Flow cytometry

Non-infected and STSV2 infected cells (approximately 3×10^7 CFU) were harvested at the indicated time points and fixed with 70% cool ethanol overnight (>12 h). The fixed cells were then collected by centrifugation at 675×*g* for 20 min and resuspended in 1 ml of PBS buffer (137 mM NaCl, 2.7 mM KCl, 10 mM $Na_2HPO_4 \times 12H_2O$, 2 mM KH_2PO_4, pH 7.4,) with 0.05% Tween-20. The cells were precipitated again and resuspended in 100 μl of staining buffer containing 40 μg/ml propidium iodide (PI). After staining for at least 30 min, the samples were analyzed for DNA content using the Amnis® ImageStreamX Mark II imaging flow cytometer (Merck Millipore, Germany). The data of 100,000 imaged cells or particles were collected from each sample and then single cells were selected and analyzed for DNA content by IDEAS data analysis software.

For sorting of the STSV2-infected cell population into populations of different sizes, MoFlo Astrios cell sorter (Beckman Coulter) was used. The sorting was carried out with a 70 μm nozzle at a pressure of 60 PSI and a differential pressure with the sample of 0.3-0.4 PSI. The calibration of the machine was carried out using Megamix-Plus SSC beads (BioCytex).

Quantitative reverse transcription PCR (RT-qPCR)

Samples from non-infected and STSV2-infected REY15A cells were collected at the indicated time points, and the total RNAs were extracted using TRI Regent (SIGMA-Aldrich, USA). The quality and quantity of the total RNAs were checked using the Eppendorf BioSpectrometer basic (Eppendorf AG, Germany) and agarose (1%) gel electrophoresis.

Quantitative reverse transcription PCR (RT-qPCR) was carried out to determine the transcriptional levels of the cell division genes during the infection process. First-strand cDNAs were synthesized from the total RNAs according to the protocol from the Maxima First Strand cDNA Synthesis Kit for RT-qPCR with dsDNase (Thermo Scientific, USA). The resulting cDNA preparations were used to evaluate the mRNA levels of the cell division proteins by qPCR, using Luna Universal qPCR Master Mix (New England Biolabs, USA) and gene specific primers (Table S1). PCR was performed in an Eppendorf MasterCycler RealPlex^4 (Eppendorf AG, Germany) with the following steps: denaturing at 95°C for 2 min, 40 cycles of 95°C 15 s, 55°C 15 s and 68°C 20 s. Relative amounts of mRNAs were evaluated using the comparative Ct method with 16S rRNA as the reference (5).

PCR amplification of the CRISPR loci

Leader proximal regions (~750 bp) of the two CRISPR loci, extending from the leader sequence to the fifth spacer (-432 to 231 for locus 1 and -424 to 239 for locus 2) were amplified. Genomes from the non-infected and STSV2-infected REY15A cells at indicated time points were extracted and 100 ng of the purified DNA were used as templates for PCR amplification. The primers used for PCR are listed in Table S1. PCR was performed using Phusion DNA polymerase (Thermo Fisher Scientific, USA) with the following steps: denaturation at 98℃ for 10 min, 20 cycles of 98℃ 10 s, 50℃ 20 s and 72℃ 1 min.

SI Figures and legends

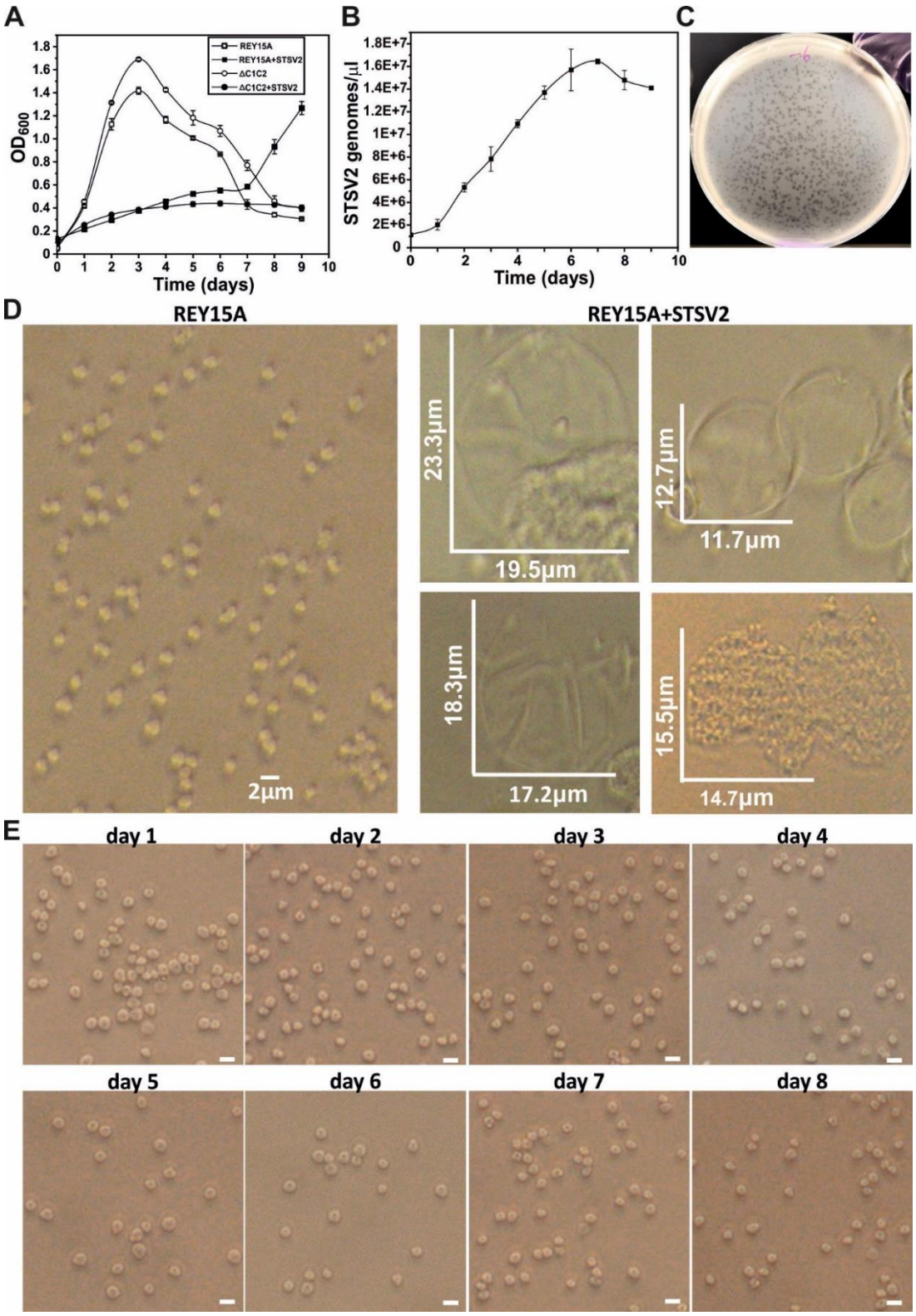

Figure S1. STSV2 infection induces growth retardation but no lysis. (A) Growth curves of non-infected and STSV2-infected REY15A and ΔCRISPR (ΔC1C2) cells. Error bars represent standard deviation from

three independent experiments. The cells were infected using a multiplicity of infection of 10. (B) Enumeration of extracellular STSV2 virions over the course of 9 days. The infected cell cultures were collected at the indicated time points and the cells were removed by centrifugation (7,000 rpm for 10min), whereas 1 μl of the supernatant was used as the template for qPCR. Error bars represent standard deviation from three independent experiments. (C) Plaque assay. Representative image of the STSV2 plaques formed on the plate of REY15A cells. The plaque assay was carried out as described in Material and Methods. The plaques are a manifestation of the slower growth of infected cells compared to the surrounding non-infected cells. (D) Representative images of the STSV2-infected giant cells. Left, non-infected REY15A cells; right, STSV2-infected REY15A cells with different sizes. The cell sizes are indicated with the corresponding scale bars. (E) Bright-field microscopy analysis of non-infected REY15A cells over the course of 8 days. There was no obvious change in the cell size during the time of experiment for non-infected cells. Bars, 2 μm.

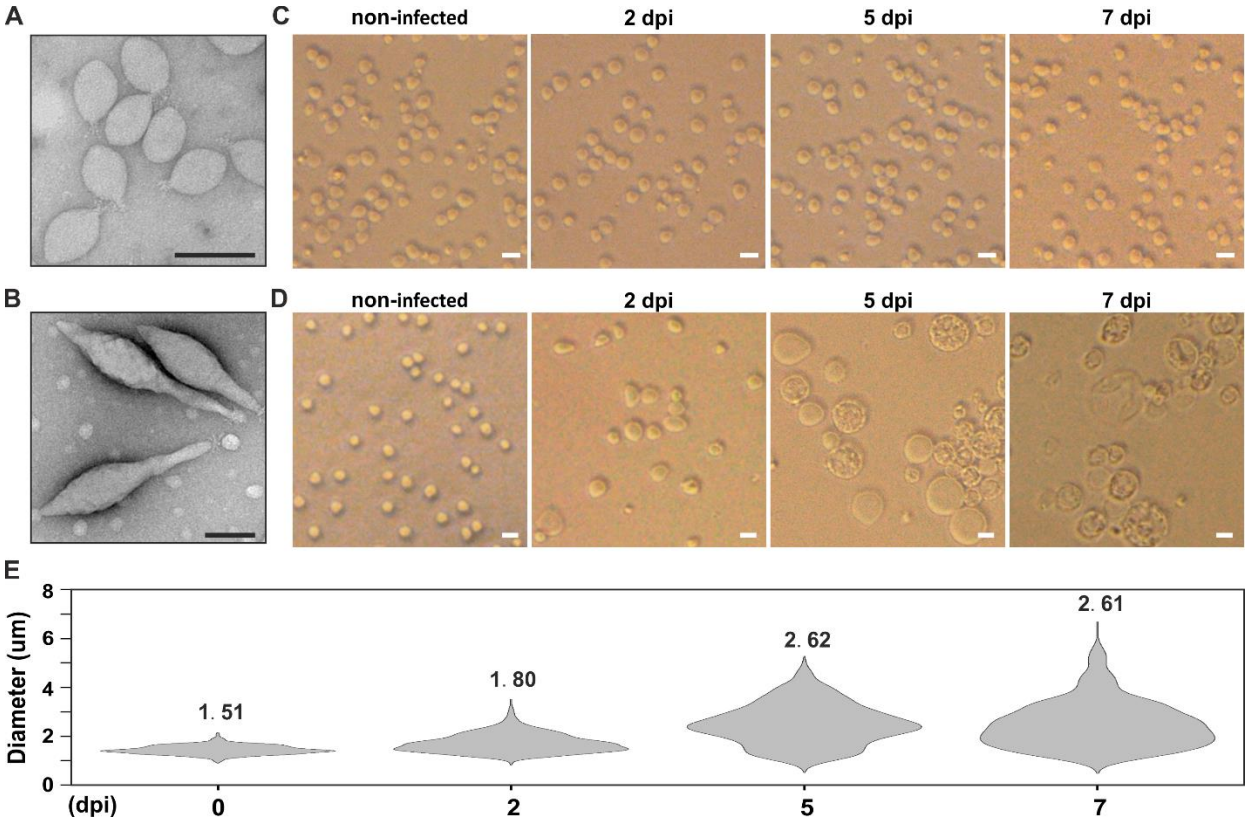

Figure S2. Effect of SSV2 and SMV1 on the size of *S. islandicus* ΔC1C2 cells. (A) Transmission electron micrograph of SSV2 virions negatively stained with 2.0% (w/v) uranyl acetate. Scale bar, 100 nm. (B) Transmission electron micrograph of SMV1 virions negatively stained with 2.0% (w/v) uranyl acetate. Scale bar, 100 nm. (C) Bright-field microscopy analysis of non-infected and SSV2-infected *S. islandicus* ΔC1C2 cells. SSV2 infection does not induce appreciable changes in cell size. Scale bars, 2 μm. (D) Bright-field microscopy analysis of non-infected and SMV1-infected *S. islandicus* ΔC1C2 cells. Similar to STSV2, SMV1 infection induces the formation of abnormally big cells. Scale bars, 2 μm. (E) Size distribution of the SMV1-infected ΔC1C2 cells during different time points after infection. The numbers above the plots represent median diameters of cells during each time point. dpi, days post infection.

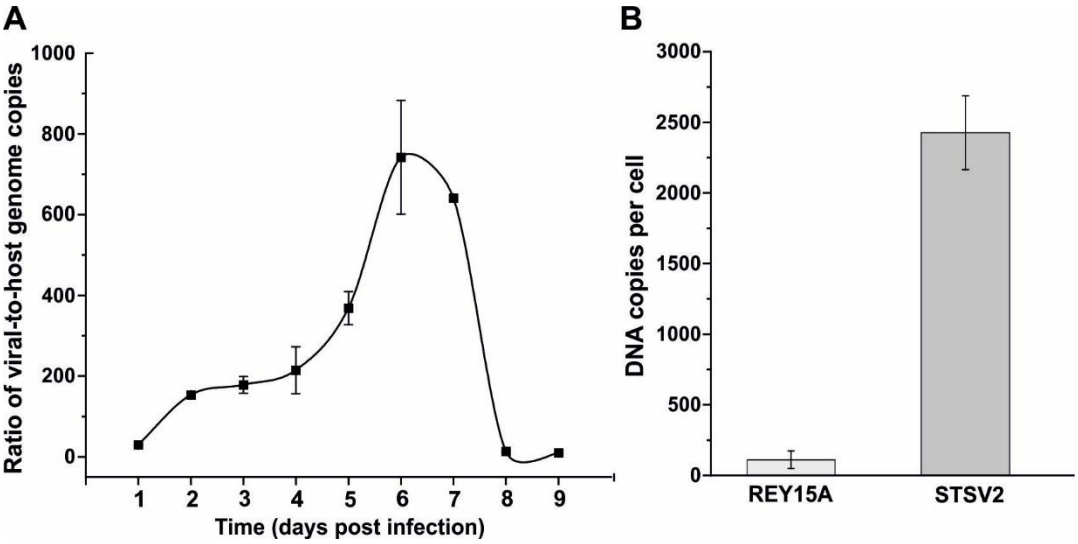

Figure S3. qPCR analysis of the viral and host DNA copy numbers in the infected cells. (A) Ratio of viral-to-host genome copies in STSV2 infected cells. STSV2-infected REY15A cells were collected at different time points post infection, the total (viral + cellular) DNA was extracted and used as a template for qPCR with chromosome (ESCRT-III-3-F/R; Table S1)- and virus (STSV2_37-F/R; Table S1)-specific primers. Plotted is the ratio between the copy numbers of the viral and cellular genomes. The error bars represent standard deviation from three independent experiments. (B) Quantification of the viral and host DNA copy numbers per cell by qPCR. The infected big cells at 6 dpi with a diameter more than 5 μm (from 6 to 16 μm, median 9.45 μm) were sorted by flow cytometry and 1,000 cells were used as the template for qPCR. Error bars represent standard deviation from three independent experiments.

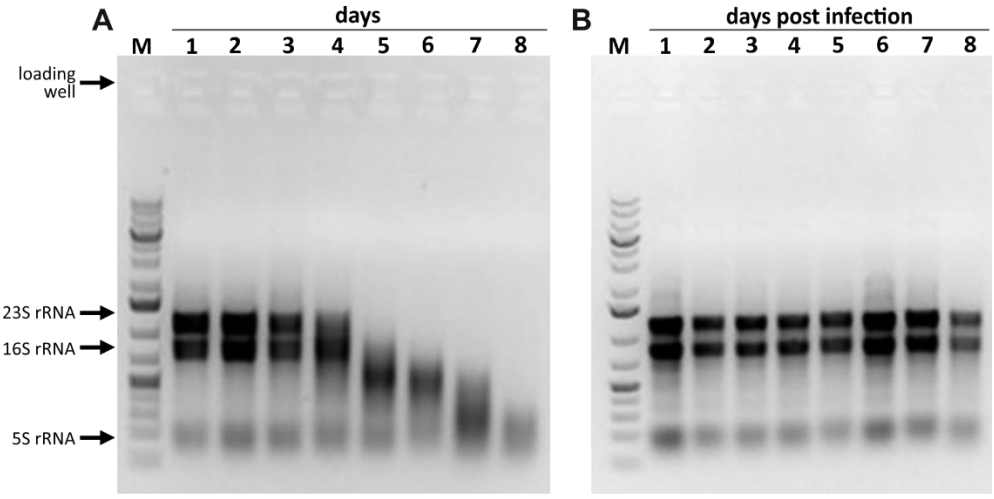

Figure S4. Determination of the quality of the RNA extracted from the non-infected (A) and STSV2-infected (B) REY15A cells. Once the non-infected cells entered the death phase (day 4), the RNA started to degrade (A). By contrast, no degradation of the RNA was observed in the STSV2-infected cells (B). M, molecular size marker.

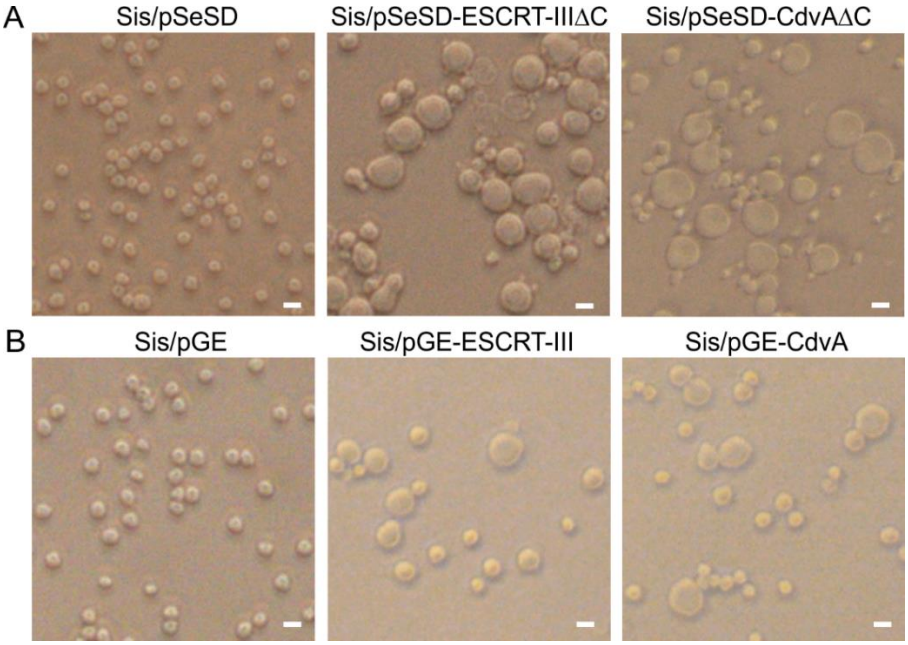

Figure S5. Overexpression of defective cell division proteins and transcriptional repression of cell division genes leads to appearance of cells with large diameters. (A) Bright-field micrographs of *S. islandicus* (Sis) cells carrying the empty pSeSD vector (control; left) as well as plasmids pSeSD-ESCRT-IIIΔC (middle) and pSeSD-CdvAΔC (right) expressing C-terminally truncated proteins ESCRT-III and CdvA, respectively. Cells with diameters of 4-5 μm can be observed in the case of both overexpression plasmids. Bars, 2 μm. (B) Bright-field micrographs of *S. islandicus* (Sis) cells carrying the empty pGE vector (control; left) as well as plasmids pGE-ESCRT-III (middle) and pGE-CdvA (right) carrying CRISPR spacers targeting transcripts of genes encoding ESCRT-III and CdvA, respectively. Cells with diameters of 4 μm can be observed in the case of both plasmids. Bars, 2 μm.

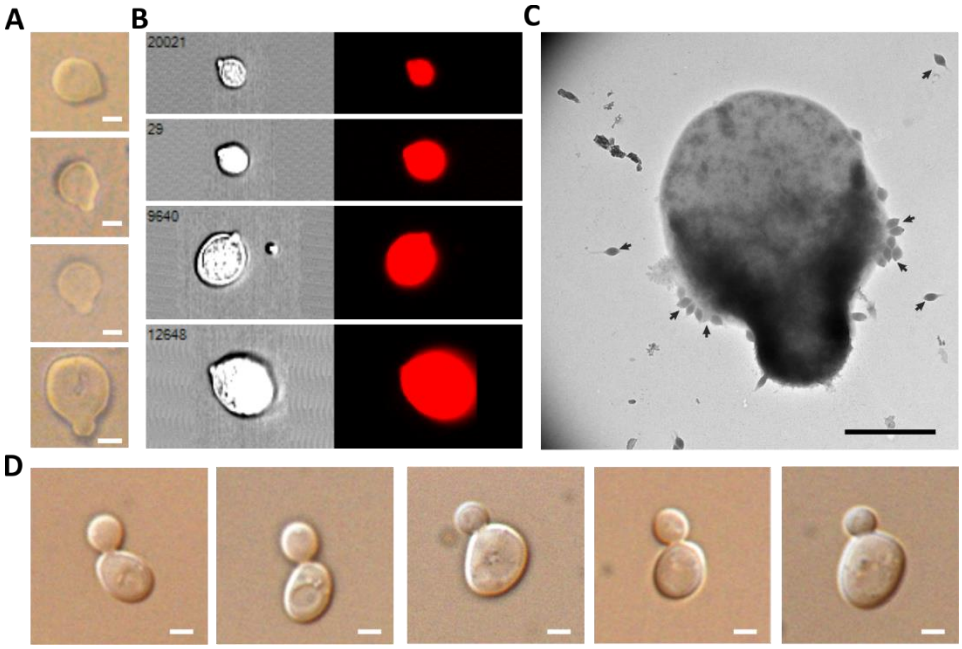

Figure S6. Asymmetric cell division by budding. (A-C) Representative images of asymmetrically dividing REY15A cells infected by STSV2 observed by bright-field microscopy (A), fluorescence microscopy following cell sorting by flow cytometry (B) and transmission electron microscopy (C). STSV2 virions attached to the cell surface are indicated with black arrows in panel C. Scale bars, 1 μm. (D) A selection of bright-field micrographs of asymmetrically dividing budding yeast. Scale bars, 2 μm.

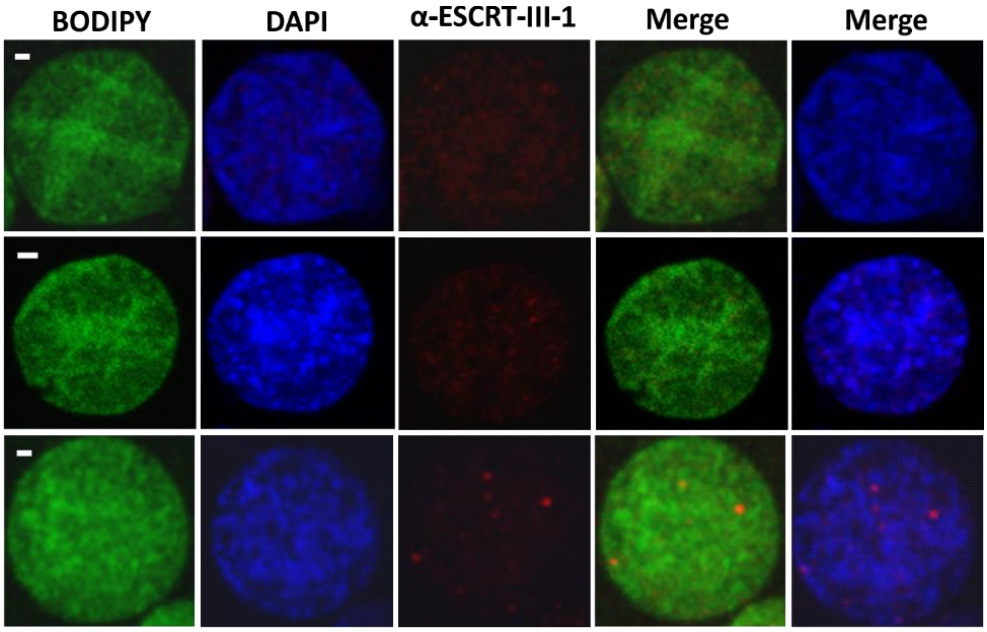

Figure S7. Fluorescence microscopy analysis of the STSV2-infected giant *S. islandicus* cells. In the absence of asymmetric division by budding, ESCRT-III-1 forms only small dot-like foci, rather than ring or spiral-like structure observed in the presence of the budding cells. Fixed cells were stained with BODIPY (green) to visualize the membrane, DAPI (blue) to visualize DNA and fluorescently labelled anti-ESCRT-III-1 antibody (red) to visualize ESCRT-III-1. Scale bars, 1 μm.

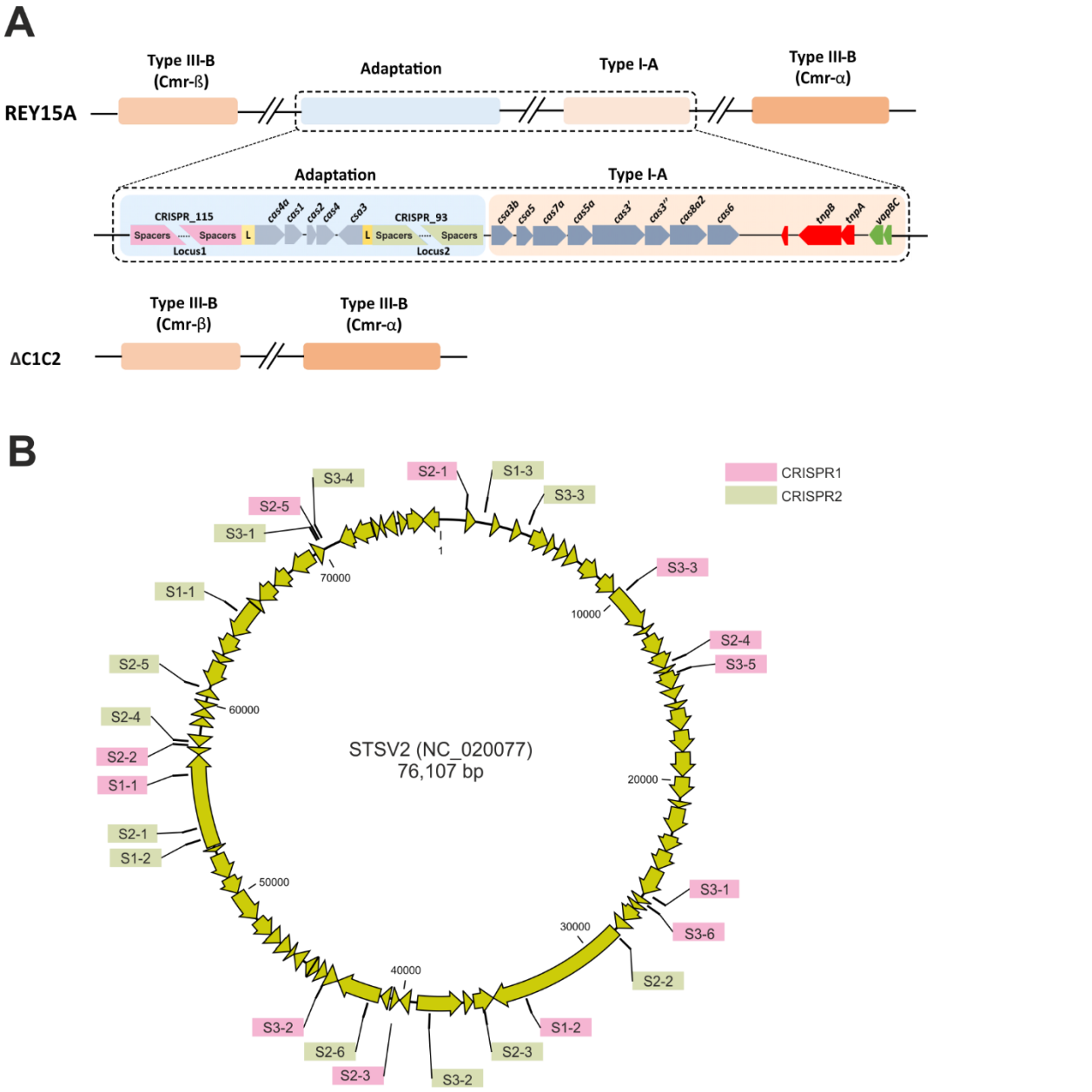

Figure S8. Development of CRISPR-dependent resistance to STSV2. (A) Overview of the CRISPR-Cas loci in *S. islandicus* REY15A (top). ΔC1C2 (bottom) is a deletion mutant, which lacks the only adaptation module, including the two CRISPR loci (pink and green, respectively), and the Type I-A interference module. L, leader sequence. (B) Distribution of the protospacers targeted by spacers present in the three STSV2-resistant REY15A strains, S1–S3. Protospacers found in the CRISPR1 and CRISPR2 loci are shown on the pink and green backgrounds, respectively.

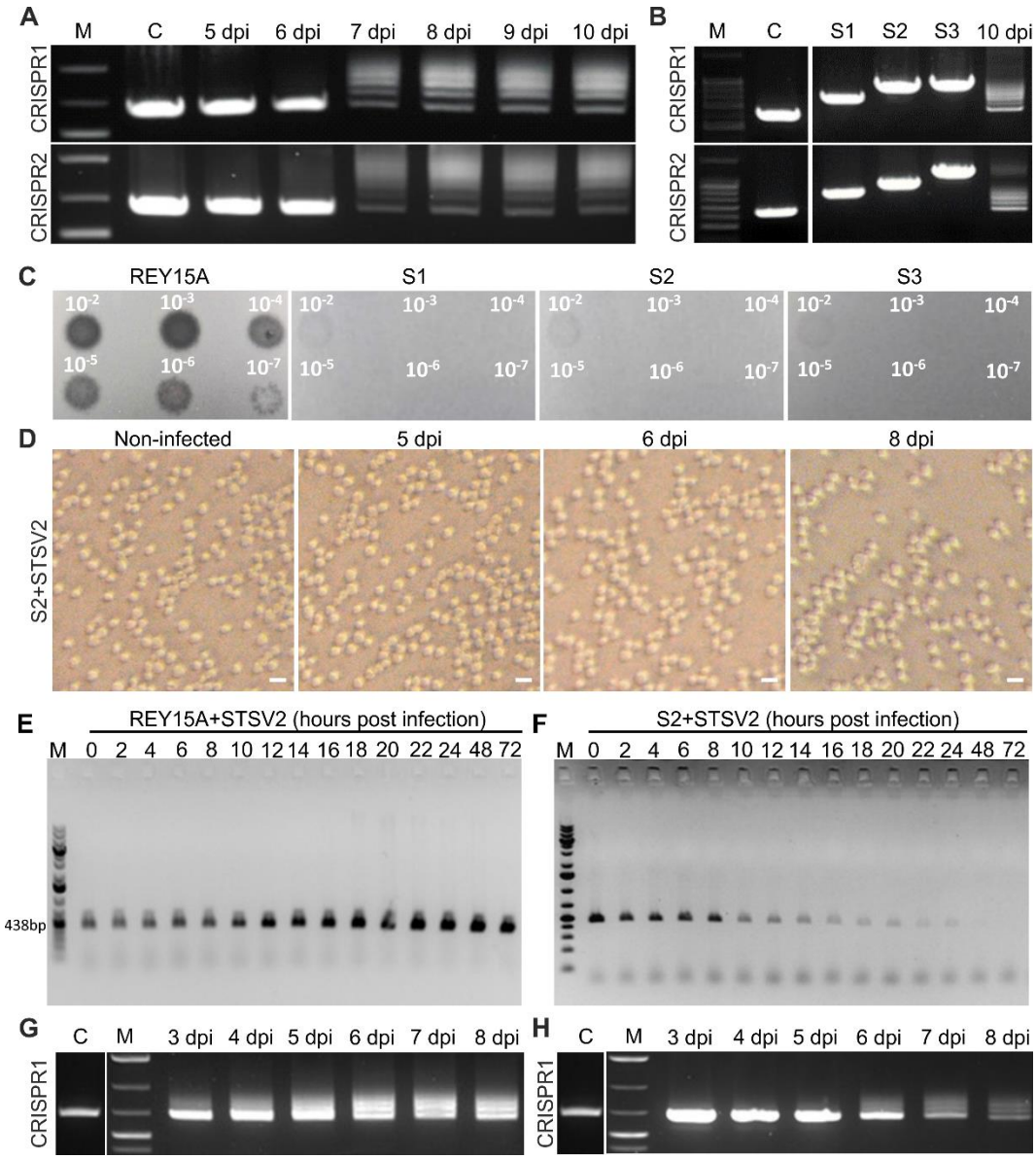

Figure S9. STSV2-infected cells develop CRISPR-based resistance. (A) Acquisition of new CRISPR spacers by STSV2-infected REY15A cells. Agarose gels show PCR products of the leader-proximal repeat-spacer units amplified from the cultures of infected cells at different time points using specific primers complementary to the leader sequence (forward primer) and the fifth spacer of the parental strain (reverse primer; Table S1). Two pairs of primers were used to amplify spacers acquired in the CRISPR loci (CRISPR1 and CRISPR2, respectively). C, positive control (PCR product obtained using the non-infected REY15A strain as a template); M, molecular size marker; dpi, days post infection. (B) Spacer content of the 3 purified clones, S1-S3, resistant to STSV2 infection. PCR amplification was performed as described in panel A. Last lane for both CRISPR1 and CRISPR2 loci shows the amplification products from the 10 dpi culture. (C) Spot test on the lawns of the parental REY15A strain and the 3 purified clones, S1-S3, resistant to STSV2 infection and carrying variable numbers of spacers. (D) Bright-field microscopy analysis of the S2 cells infected with STSV2. Scale bars: 2 μm. (E, F) PCR amplification of the STSV2 genome in REY15A cells without (E) and with (F) CRISPR spacers (S2). Around 0.7×10^8 infected cells were collected, pelleted and washed 3 times with fresh medium (7,000 rpm, 10 min) to remove the extracellular

virus particles. Finally, the cells were re-suspended in 400 µl of fresh medium and 2 µl were used as a template for PCR with the primers specifically targeting the gene encoding the coat protein (STSV2_37-F/R; Table S1) of the virus. (G,H) Spacer content of the normal-sized (G) and big (H) cells sorted by flow cytometry. PCR amplification was performed as described in panel A.

SI Videos

Supplementary video 1. 3D reconstruction of a STSV2-infected REY15A cell in the process of asymmetric cell division by budding. The cells were stained with DAPI and observed using Leica SP8 immunofluorescence microscope. The images were analyzed by the Leica Application Suite X (LAS X) software and displayed in the Volume mode. The color scale indicates the Z-depth. The 3D video was obtained by rotation around Y-axis and then the X-axis with 1.5 times enlargement.

SI Table

Table S1. Strains and oligonucleotides used in this study.

Strains		
Strain	**Genotype**	**Source**
S. islandicus REY15A	Wide type	(6)
ΔC1C2	REY15A *ΔpyrEF ΔlacS Δcrispr1 Δcrispr2*	(2)
Sis/pSeSD-CdvAΔC	CdvAΔC over-expression	(3)
Sis/pSeSD-ESCRT-III ΔC	ESCRT-IIIΔC over-expression	(3)
Sis/pGE-CdvA	CdvA knockdown strain	(7)
Sis/pGE-ESCRT-III	ESCRT-III knockdown strain	(7)
Saccharomyces cerevisiae Y2H Gold	*MATa, trp1-901, leu2-3, 112, ura3-52, his3-200, gal4Δ, gal80Δ, LYS2 : : GAL1UAS-Gal1TATA-His3, GAL2UAS-Gal2TATA-Ade2 URA3 : : MEL1UAS-Mel1TATA AUR1-C MEL1*	Clontech
S1	REY15A clone 1 with CRISPR spacers against STSV2	This study
S2	REY15A clone 2 with CRISPR spacers against STSV2	This study
S3	REY15A clone 3 with CRISPR spacers against STSV2	This study
Oligonucleotides		
Name	**Sequence (5'-3')**	**Source**
16S-F	GAATGGGGGTGATACTGTCG	(8)
16S-R	TTTACAGCCGGGACTACAGG	(8)
Locus1-F	GTCCATAGGAGGACCAGC	(9)
Locus1-R	CCAACCCCTTAGTTCCTCCTC	(9)
Locus2-F	GTTCCTTCCACTATGGGACTA	(9)
Locus2-R	CGTCACTGACACCATATTTAT	(9)
STSV2_37-F	CTTCAGATCCAGTAAGAAGAG	This study
STSV2_37-R	GTGGTAATGCTGTACTGTTAG	This study
CdvA-F	GGTTCTTCTATCTTGACTATGG	This study
CdvA-R	GTATAATTCCTCTAACGCTCTC	This study
ESCRT-III-F	GTAGTTCCTGCGGTAGTAG	This study
ESCRT-III-R	CTTGACGATTGCTCTATTGG	This study
Vps4-S-F	CCAGAATCAGTAGCGAGAAC	This study
Vps4-S-R	AGTTGTACCATCTCCTCCAC	This study
ESCRT-III-1-F	GCTCCATGATTAGTAGGCTTG	This study
ESCRT-III-1-R	CTGCTACCTCATTAGCGTAC	This study
ESCRT-III-2-F	GGTCGTAGAATCTCAGATGTC	This study
ESCRT-III-2-R	CTGAGTTGTACTTGCTCTAGG	This study
ESCRT-III-3-F	GCTGAGCTGCTAATAGACG	This study
ESCRT-III-3-R	CTCAGACTCTCTAGCAACC	This study
TBP-F	GTGGCAACAGTTACGTTAGAG	This study
TBP-R	CCTTGGGCTGTTCTAATCTG	This study

SI References

1. Uldahl KB, Walk ST, Olshefsky SC, Young MJ, & Peng X (2017) SMV1, an extremely stable thermophilic virus platform for nanoparticle trafficking in the mammalian GI tract. *J Appl Microbiol* 123(5):1286-1297.
2. Gudbergsdottir S*, et al.* (2011) Dynamic properties of the Sulfolobus CRISPR/Cas and CRISPR/Cmr systems when challenged with vector-borne viral and plasmid genes and protospacers. *Mol Microbiol* 79(1):35-49.
3. Liu J*, et al.* (2017) Functional assignment of multiple ESCRT-III homologs in cell division and budding in Sulfolobus islandicus. *Mol Microbiol* 105(4):540-553.
4. Zhang C*, et al.* (2019) Cell Structure Changes in the Hyperthermophilic Crenarchaeon Sulfolobus islandicus Lacking the S-Layer. *mBio* 10(4):e01589-01519.
5. Schmittgen TD & Livak KJ (2008) Analyzing real-time PCR data by the comparative C(T) method. *Nat Protoc* 3(6):1101-1108.
6. Guo L*, et al.* (2011) Genome analyses of Icelandic strains of Sulfolobus islandicus, model organisms for genetic and virus-host interaction studies. *J Bacteriol* 193(7):1672-1680.
7. Liu J*, et al.* (2021) Archaeal extracellular vesicles are produced in an ESCRT-dependent manner and promote gene transfer and nutrient cycling in extreme environments. *bioRxiv* doi: https://doi.org/10.1101/2021.02.09.430445.
8. Sun M*, et al.* (2018) An Orc1/Cdc6 ortholog functions as a key regulator in the DNA damage response in Archaea. *Nucleic Acids Res* 46(13):6697-6711.
9. Erdmann S*, et al.* (2014) A novel single-tailed fusiform Sulfolobus virus STSV2 infecting model Sulfolobus species. *Extremophiles* 18(1):51-60.